

Simulating heart valve mechanical behavior for planning surgical repair

by

Peter E. Hammer

A dissertation submitted to the faculty of
Tufts University
in partial fulfillment of the requirements for the degree of

Doctor of Philosophy
in
Biomedical Engineering

February 2011

Research Committee:

Prof. Robert D. Howe
School of Engineering and Applied Sciences, Harvard University

Prof. Sergio Fantini
Department of Biomedical Engineering, Tufts University

Pedro J. del Nido, M.D.
Department of Cardiac Surgery, Children's Hospital Boston

Prof. A. Benjamin Perlman
Department of Mechanical Engineering, Tufts University

Prof. Mark Cronin-Golomb
Department of Biomedical Engineering, Tufts University

Abstract

Heart valves are functionally complex, making surgical repair difficult. Simulation-based surgical planning could facilitate repair, but current finite element (FE) studies are prohibitively slow for rapid, clinically-oriented simulations. An anisotropic, nonlinear mass-spring (M-S) model is presented to approximate the membrane behavior of heart valve leaflet tissue, and it is coupled with a fast method for simulating valve dynamics. An efficient FE model is also described for simulating valve leaflets. The speed-accuracy tradeoff between the FE and M-S models is quantified so that the strength of each method can be leveraged where appropriate. The FE model is applied to study a generalized aortic valve repair technique that incorporates graft material into the native valve, where the graft has significantly different mechanical properties than native leaflets. Results show that the graft must be larger than the native leaflets and predicts optimal graft height and width. The M-S method is applied to fully image-based models of the mitral valve to simulate valve closure and loading for fast applications like intraoperative surgical planning. This model is used to simulate a technique used in valve repair and to assess the importance of chordae in determining the closed configuration of the valve. Direct image-based comparison was used for validation. Results of M-S model simulations showed that it is possible to build fully image-based models of the mitral valve and to rapidly simulate closure with sub-millimeter accuracy. Chordae, which are presently difficult to image, are shown to be strong determinants of the closed valve shape.

Acknowledgements

First I would like to thank Pedro del Nido and Rob Howe for outstanding advising and mentorship throughout my studies. I have learned as much from their models of dedication and management style as from the knowledge that they have imparted through mastery of their fields. I also thank my committee members at Tufts - Sergio Fantini, Benjamin Perlman and Mark Cronin-Golomb - for their guidance.

I am grateful for the support of colleagues at Children's Hospital Boston. Doug Cowan generously provided financial support and valuable advice. Doug Perrin contributed ideas and discussions central to my research, and Nikolay Vasilyev shared his clinical knowledge and surgical expertise. I also thank Patricia Dunning and Fred Fahey for help with CT imaging. I also thank past and present colleagues in the Harvard Biorobotics Lab, including Laura Brattain, Leif Jentoft, Petr Jordan, Sam Kesner, Paul Novotny, Rob Schneider, Mahdi Tavakoli, Neil Tenenholz, and Shelten Yuen. I would like to thank Professor Michael Sacks of the University of Pittsburgh for his contributions and helpful discussions on heart valve biomechanics. I acknowledge funding from the National Institute of Health and from the Tufts Graduate Student Council.

Finally, I am grateful to my family for their unwavering support and understanding throughout my years of study.

Table of Contents

1 Introduction.....	2
2 Background	7
2.1 Overview of heart valves	7
2.2 The mitral valve	10
2.2.1 Structure and function of the normal valve.....	10
2.2.2 Pathology	13
2.3 The aortic valve.....	15
2.3.1 Structure and function of the normal valve.....	15
2.3.2 Pathology	17
2.4 Valve repair versus replacement	17
2.5 Computational modeling of heart valves	19
2.5.1 Previous computational studies of the mitral valve	19
2.5.2 Previous computational studies of the aortic valve.....	23
3 Anisotropic mass-spring model of heart valve tissue: comparison with a finite element model.....	27
3.1 Introduction.....	27
3.2 Methods.....	30
3.3 Results.....	41
3.4 Discussion	51
4 Finite element model of aortic valve surgical repair using grafted pericardium	59
4.1 Introduction.....	59

4.2 Methods.....	60
4.3 Results.....	67
4.4 Discussion	71
5 Image-based mass-spring model of the mitral valve	76
5.1 Introduction.....	76
5.2 Methods.....	78
5.3 Results.....	85
5.4 Discussion	93
6 Conclusions and future work.....	100
Appendix.....	104
References	107

List of Tables and Figures

Figure 1.13
Figure 2.18
Figure 2.29
Figure 2.310
Figure 2.413
Figure 2.516
Figure 3.133
Figure 3.234
Table 3.142
Figure 3.343
Figure 3.445
Figure 3.547
Figure 3.648
Figure 3.749
Table 3.250
Table 3.351
Figure 3.853
Figure 4.161
Figure 4.263
Figure 4.364
Figure 4.469
Figure 4.570
Figure 4.674
Figure 4.774
Figure 5.178
Figure 5.280
Figure 5.380
Figure 5.481
Figure 5.582
Table 5.182
Figure 5.684
Table 5.286
Figure 5.786
Figure 5.887
Figure 5.989
Figure 5.1090
Figure 5.1191
Figure 5.1292

**Simulating heart valve mechanical behavior
for planning surgical repair**

1 Introduction

Serious heart valve disease affects 1 in 40 adults in the United States [1], and surgeons perform approximately 100,000 heart valve operations per year in the U.S. [2]. The consensus has been growing that valves should be repaired rather than replaced with prosthetics whenever possible [3], [4]. However valve reconstruction is technically difficult and outcomes are highly dependent upon the experience of the surgeon [5]. Consequently, small centers often do not accumulate sufficient experience with valve repair to apply the techniques as widely as do large centers that have surgeons specializing in valve repair [6].

One of the main difficulties of valve repair is that valve tissues must be surgically altered during open heart surgery such that the valve opens and closes effectively after the heart is closed and blood flow is restored. In order to do this successfully, the surgeon must essentially predict the displacement and deformation of geometrically and biomechanically complex valve leaflets and the structures to which they attach. While difficult for humans, this task is well suited for computers. A computer based surgical planning system could potentially extract relevant valve anatomy from pre- or intra-operative medical images and use it to create a computational mesh. This mesh could then be modified by the surgeon through a graphical interface to test potential surgical repair options. Adequacy of a given surgical repair option could then be assessed by using

computational modeling methods to simulate the opening and closing of the valve under typical physiological conditions (Fig. 1).

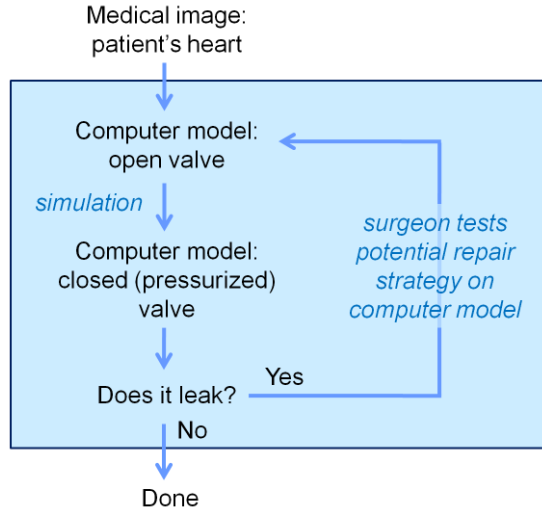


Figure 1.1 Simulation-based surgical planning system for heart valve repair.

Computational modeling based on the finite element (FE) method is a powerful numerical approach for structural analysis. It has seen widespread use in the design of manufactured parts, and it is this application that has largely driven the development of FE software. Current commercial FE analysis programs are very good at meshing parts from computer-aided design specifications and estimating strain and stress fields throughout the mesh. Most manufactured parts are made from materials that undergo small strains under normal operating conditions, and the dimensions of the parts are typically known to a high degree of precision. Consequently, analysis methods have evolved to estimate stress and strain fields with high precision. This emphasis on precision comes at the expense of computation time, which is often quite large for analysis of complex structures.

Computational methods have been applied to study both the mitral and aortic valves. These studies have provided insights into the function of normal and diseased valves and have been used to assess prosthetic valves as well as surgical repair techniques. Most of these analyses have relied on commercial FE analysis software and have been subject to two main limitations imposed by the software. First, generic and idealized models of valve geometry have been assumed in order to use commercial mesh generation software designed primarily for parts that can be expressed using analytically specified shapes, such as manufactured parts. Second, simulations require long computation times, reflecting the prioritization of precision and accuracy over computation time. Both of these limitations preclude the direct application of these simulation methods for surgical planning applications where patient-specific valve geometry and fast computation times are essential.

Two surgical planning paradigms guide this work. *Pre-operative* surgical planning involves running such simulations prior to surgery based on images acquired during a pre-operative hospital visit. *Intra-operative* surgical planning entails running simulations in the operating room during the heart valve repair surgery, with the ability to incorporate valve dimensions or other information acquired through direct visual or manual access to the valve during surgery. This approach imposes stricter requirements on simulation time, since simulations must be run during time-sensitive surgical cases. However, even pre-operative

surgical planning implies limits on computation time, as there is a practical limit to how much time a busy surgeon can spend interacting with a computer model.

The goal of this thesis is to design and develop computer-based tools for simulation of heart valve closure for use in planning surgical repair. There are three fundamental requirements for the simulation environment. Modeling methods must (1) accommodate description of valve anatomy by medical images, (2) incorporate large deformation and biomechanically complex behavior of valve tissues, and (3) operate within speed and accuracy ranges appropriate for the application. In order to meet these requirements, I have developed methodologies for pressurizing and imaging heart valves along with software for producing computational meshes from these images. I then developed software for rapidly simulating the dynamics of the meshes, implementing both a FE method of computing material deformation and a mass-spring (M-S) model, a faster but more approximate method based on techniques used in computer graphics. I then used these methods to simulate the closing and loading of aortic and mitral valves and techniques for their repair.

In Chapter 2, I describe the function and diseased states of the mitral and aortic valves and discuss surgical options for treatment. I also survey prior work in computational modeling of each valve. In Chapter 3, I present an M-S model to approximate the nonlinear and anisotropic mechanical behavior of heart valve leaflet tissue. An efficient FE membrane model is also described, and the two

models are compared in terms of speed and accuracy. In Chapter 4, I use the FE membrane model described in Chapter 3 to provide general guidelines for sizing graft material for aortic valve repair. In Chapter 5, I describe a method for developing fully image based computational meshes of the mitral valve, and I use the meshes to study fundamental requirements for predictive modeling of the valve, including the role of chordae and the sensitivity of simulation results to parameters describing model geometry and tissue behavior. A simple surgical repair, replacing a native chord with a synthetic one and varying its length, is then simulated, and simulation results are validated by directly comparing the predicted closed valve surface to images of the closed valve after performing the same repair on a mitral valve of an isolated heart. In Chapter 6, I conclude and discuss future directions for this work.

2 Background

2.1 Overview of heart valves

The mammalian heart is essentially two pulsatile pumps operating in sync, side by side, in the same organ (Fig. 2.1). The ventricles, one on the left and one on the right side of the heart, have thick muscular walls that cyclically contract and relax to create pressure gradients throughout the circulatory system. Heart valves, opened and closed by these pressure gradients, control the direction of blood flow through the heart. Both right and left ventricles have an inlet valve, or atrioventricular valve, which opens to allow the ventricle to fill and then closes as the ventricle contracts so that the blood must leave via a different route. Both ventricles also have an outflow valve, or semilunar valve, which opens to allow ejected blood to leave the ventricle, then closes to maintain pressure downstream in the outflow vessel while the ventricle relaxes and refills. The two pumps maintain blood circulation, with the right heart pumping deoxygenated systemic blood to the lungs and the left heart pumping the oxygenated blood returning from the lungs out to the systemic circulation.

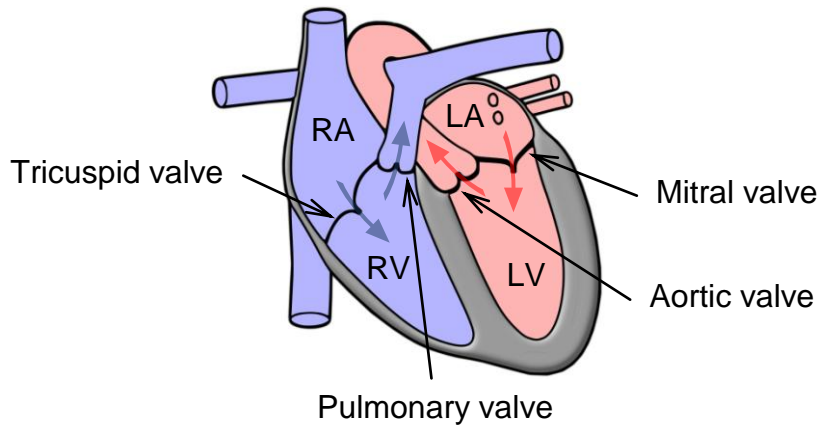


Figure 2.1 Blood flow through the heart. Oxygenated blood (shown in red) returns from the lungs to the left atrium (LA) after which it passes through the mitral valve into the left ventricle (LV). The LV pumps the blood through the aortic valve to perfuse the systemic circulation. Deoxygenated blood (shown in blue) returns from the systemic circulation to the right atrium (RA) after which it passes through the tricuspid valve into the right ventricle (RV). The RV pumps deoxygenated blood through the pulmonary valve to the lungs.

The atrioventricular valves are structurally somewhat different than the semilunar valves. Each atrioventricular valve consists of an irregular ring of membranous tissue that attaches to the heart wall over a ring-shaped region called the annulus (Fig 2.2). Distinct lobes of this membranous tissue are referred to as leaflets. The free edges of the leaflets are tethered by thin tendons, the chordae tendineae, to the papillary muscles, which are specialized muscles on the inside of the ventricle wall. The right atrioventricular valve is called the tricuspid valve,

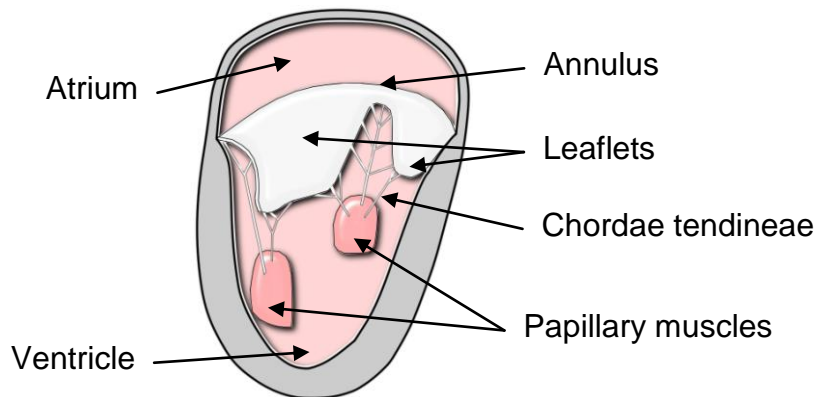


Figure 2.2 Major structures of an atrioventricular valve include the leaflets, annulus, chordae tendineae, and papillary muscles.

with the name reflecting the three-leaflet structure. The left atrioventricular valve is called the mitral valve because the two-leaflet structure resembles a miter, a type of headgear worn by Catholic bishops. The semilunar valves each consist of three half-moon-shaped leaflets that attach to the walls of their respective outflow vessels (Fig. 2.3). The region at which two adjacent leaflets join and meet the vessel wall is called a commissure. Semilunar valves lack the tethering chordae of the atrioventricular valves, instead gaining support from their coronet-shaped curve of attachment to the outflow vessel. The left semilunar valve is called the aortic valve, reflecting its location in the ascending aorta, and the right semilunar valve is called the pulmonary valve, taking its name from pulmo, the Latin word for lung.

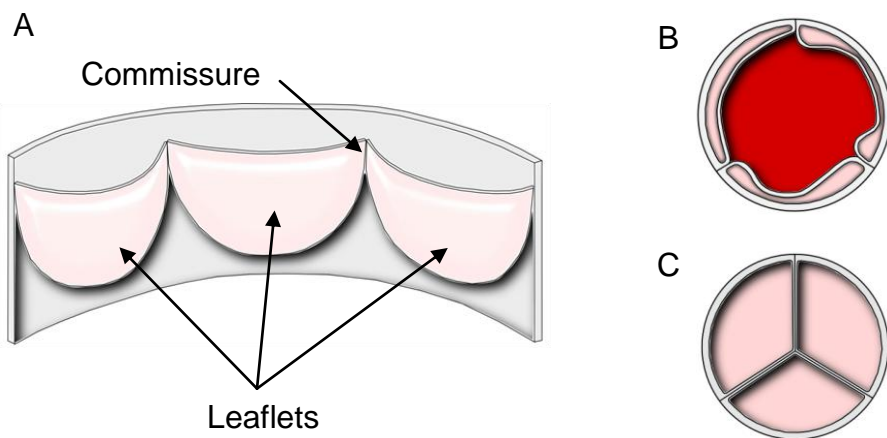


Figure 2.3 A semilunar valve shown (A) by axially cutting outflow vessel between two leaflets and unrolling, (B) from top view of transverse section of outflow vessel distal to the open valve, and (C) from top view of transverse section of outflow vessel distal to the closed valve.

An important difference between the right and left hearts is that the left heart typically achieves a peak pressure over the cardiac cycle that is about six times that of the right. Consequently, the two valves on the left side of the heart are subject to much higher loads than those on the right heart. In fact, the majority of valve disease involves the valves of the left heart [7],[8],[9]. For this reason, only the valves of the left heart, the mitral and aortic valves, are considered in the remainder of this work.

2.2 The mitral valve

2.2.1 Structure and function of the normal valve

The ring of tissue comprising the mitral valve leaflets is generally considered to consist of two leaflets, the anterior and posterior (Fig. 2.4). The anterior leaflet

typically consists of a single broad lobe whose ventricular surface (underside) forms part of the LV outflow tract. The remainder of the leaflet ring is called the posterior leaflet and typically consists of 3 or more distinct lobes, the largest of which opposes the anterior leaflet. The leaflets contain preferentially oriented collagen fibers that impart anisotropic behavior to the tissue [10]. Furthermore, the collagen fibers have a crimped structure which makes the fibers relatively distensible under small stresses, as the crimp “straightens”. Higher levels of stress cause the fibers to fully extend and result in an abrupt stiffening of the fibers. This gives the leaflets a nonlinear stress-strain relationship [10].

The branching network of chordae tendineae plays a crucial role in valve function. Chordae that connect the free edges of the leaflets to the papillary muscles are referred to as primary chordae, and their main role is to tether the leaflets to prevent their buckling upward toward the left atrium as pressure across the valve rises. Chordae also tether the ventricular surface of the leaflets to the papillary muscles. These are referred to as secondary chordae, and they have been reported to play a role in determining LV shape and function [11] [12]. Two secondary chordae of the anterior leaflet, referred to as strut chords, have the largest cross section of all the chordae and have been reported to play a role in forming flow channels during LV filling and ejection and to prevent the anterior leaflet from blocking the outflow tract during systole [13].

The papillary muscles anchor the chordae tendineae to the LV wall. It has been hypothesized that they play a role in the dynamics of valve closure and in cardiac function, although studies of the timing and magnitude of their contraction have shown contradictory results [14]. It is generally agreed that they contract during systole, and this might serve to take up slack in the chordae as the ventricle shortens axially during systole, keeping the surface of the closed valve from prolapsing into the left atrium [15].

Proper function of the mitral valve depends on complex interaction among the leaflets, chordae, papillary muscles and LV. During diastole, the LV fills with blood, passively dilating the ventricle and the annulus. Toward the end of the ventricular filling phase, the blood passing through the mitral valve decelerates causing a pressure gradient that acts to close the mitral valve [16]. The LV wall contracts during ventricular systole, causing a sharp rise in LV pressure. The closed mitral valve prevents backflow of blood into the left atrium, and the aortic valve remains closed until the LV pressure reaches the pressure in the aorta. When LV pressure exceeds aortic pressure, the aortic valve opens and blood is propelled into the aorta.

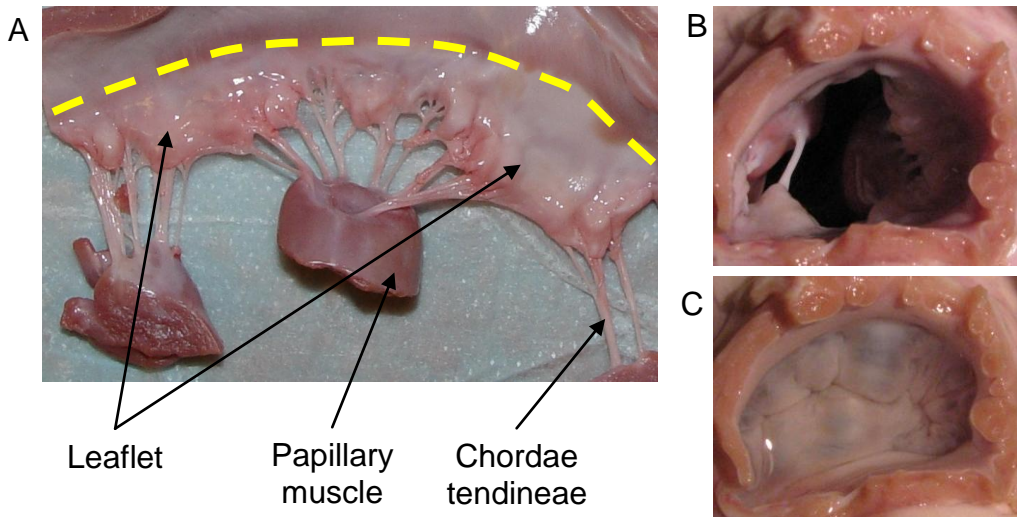


Figure 2.4 (A) Excised porcine mitral valve. The leaflets attach to the heart wall at a ring shaped region called the annulus (yellow dashed line). The free edges of the leaflets are tethered by the chordae tendineae to the papillary muscles which protrude from the inside surface of the left ventricle. (B) Top view of the open mitral valve, with the left atrium cut away. (C) Top view of the closed mitral valve after pressurizing the left ventricle with saline.

2.2.2 Pathology

Diseases of the mitral valve can be broadly classified as either inhibiting atrioventricular blood flow or allowing retrograde atrioventricular blood flow. These conditions are referred to as mitral stenosis (MS) and mitral regurgitation (MR), respectively.

MS can be caused by rheumatic heart disease, calcification of the leaflets and annulus, infective endocarditis, systemic lupus erythematosus, rheumatoid arthritis, and carcinoid heart disease. The three surgical options available for patients with MS are catheter-based balloon dilatation of the mitral valve, surgically cutting the mitral leaflet commissures, and mitral valve replacement.

Significant MR occurs in about 2% of the population with a similar prevalence in males and females [17]. The cause of MR can be either structural or functional. Structural causes include malformations or abnormal tissue properties of valve components, while functional causes refer to those resulting from abnormal heart function, including dilation of the left ventricle and dislocation of a papillary muscle following myocardial infarction. The most common causes of MR in the United States are myxomatous degeneration, chordal rupture, rheumatic heart disease, infective endocarditis, prior heart attack, untreated high blood pressure, and congenital heart defects. If left untreated, moderate to severe MR can lead to heart failure. The only effective treatment is surgery, and the two surgical options are repair of the native valve tissues and replacement of the valve with a prosthesis. A common surgical repair technique is annuloplasty, where a rigid ring is sewn onto the mitral valve annulus in order to reduce or fix annular size. Other repair techniques include leaflet resection or grafting, commissurotomy to relieve restricted leaflet mobility, and shortening, transfer or replacement of chordae.

2.3 The aortic valve

2.3.1 Structure and function of the normal valve

The three leaflets of the normal aortic valve, while generally semicircular in shape, can exhibit significant interindividual and intraindividual variation in both shape and size [18]. The leaflet tissue, as for the mitral valve, contains preferentially oriented collagen fibers that give the leaflets an anisotropic nonlinear stress-strain relationship [10]. The aortic root, to which the leaflets attach, connects the LV outflow tract to the proximal ascending aorta and exhibits significant elastic stretch over the physiological range of intravascular pressure. The root contains three bulges, or sinuses, one behind each leaflet (Fig 2.5). Two of the three sinuses serve as origins of the coronary arteries. The leaflets are named for the coronary artery that originates in its adjacent sinus. They are designated as the right-, left-, and non-coronary leaflets. The sinuses are believed to play a role in valve closure and in reducing stress in the leaflets where they attach to the root [19].

The function of the aortic valve, like the mitral, depends on blood flow dynamics as well as on the movement of the structures to which the valve components attach. The coronet shaped annulus of the aortic valve is part of the highly elastic aortic root, so the annulus passively dilates and shrinks in response to changes in aortic pressure throughout the cardiac cycle. When the aortic root is exposed to atmospheric pressure as during open heart surgery, its diameter is much smaller than its range of in vivo diameters. In this state, there is significant

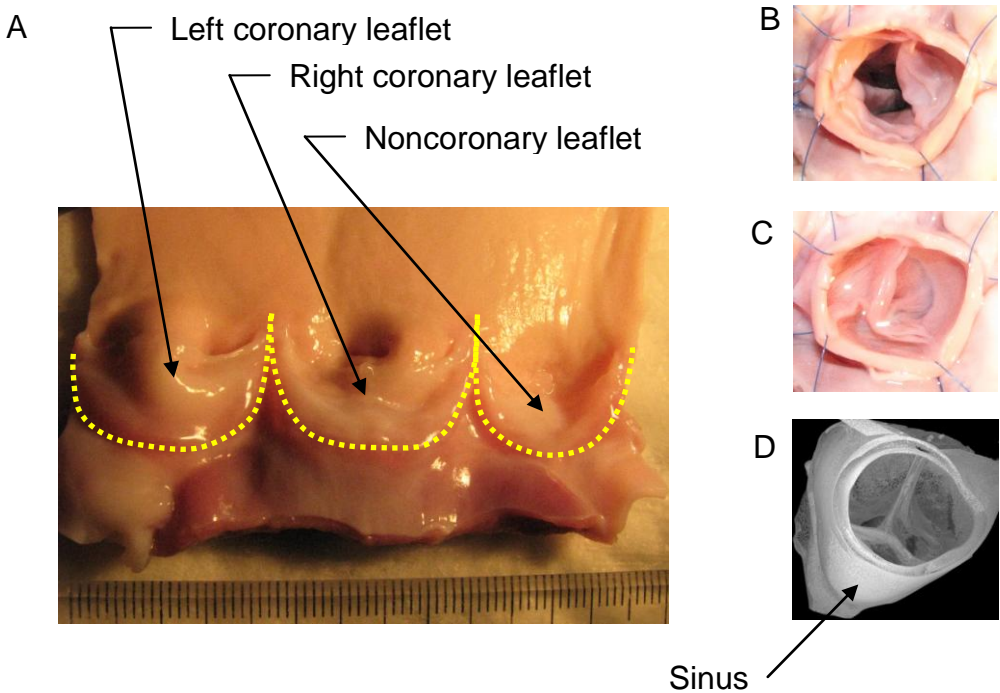


Figure 2.5 Porcine aortic valve. (A) Aorta has been cut axially between the left and non-coronary leaflets and laid flat. Coronet-shaped annulus is shown in yellow. (B) Aorta has been cut transversely, exposing the open valve. (C) Aorta has been cut transversely, exposing the closed but unpressurized valve. (D) Micro CT scan of aortic valve and root loaded by 80 mmHg of pressure.

redundancy in free edge length of the closed leaflets (Fig. 2.5C). Under physiological pressures, the valve closes with minimal redundancy of the leaflet edges due to the larger caliber of the pressurized aortic root (Fig. 2.5D).

2.3.2 Pathology

As for the mitral valve, malfunction of the aortic valve can also be classified as either restricting flow or allowing backflow. These are referred to as aortic stenosis (AS) and aortic regurgitation (AR), respectively. AS is the most common valvular disease requiring surgery [20]. Common causes of AS include calcification, congenital bicuspid valve, rheumatic valve disease and congenital AS. AR can be caused by age-related degeneration of the leaflets, endocarditis, rheumatic fever, congenital defects, and aortic enlargement associated with chronic hypertension. It can also be caused by a leaflet tear following balloon dilation of AS. As for the mitral valve, surgery is the only effective treatment, and surgical options are repair of the valve tissues or valve replacement with a prosthetic valve. Surgical repair techniques include reconstruction of the leaflets and/or commissures with autologous pericardium, aortic root reconstruction, thinning of the leaflets, and annuloplasty.

2.4 Valve repair versus replacement

Since the first artificial heart valve was implanted in the 1950's, there have been almost three million prosthetic valves implanted worldwide [21]. Currently available prosthetic valves can be classified as either mechanical or bioprosthetic. Mechanical valves are fabricated from synthetic materials, and can be extremely durable, often lasting 30 years or more [22]. A disadvantage of mechanical valves is their thrombogenicity, and patients with mechanical valves typically require

lifelong anticoagulant therapy. Bioprosthetic valves use biological materials, such as valve or vessel tissue from a donor or an animal. Bioprosthetic valves often do not have the problem with thrombogenicity, but they are less durable than mechanical valves, typically lasting from ten to fifteen years in adults [22]. In children, bioprosthetic valves tend to wear out even sooner, and neither bioprosthetic nor mechanical valves can accommodate patient growth.

Surgical repair of the mitral valve has been shown to result in better outcomes than valve replacement for common forms of MR [6] [23] [24] [25] and current surgical guidelines encourage repair over replacement whenever possible [26]. However, rates of mitral valve replacement are still high, and a primary reason is that many cardiac surgeons do not have the experience and specialized skills to consistently repair valves with complex cases of MR [6]. A tool which could help surgeons plan effective surgical repair strategies could increase the overall repair rate, resulting in lower overall morbidity and mortality for heart valve surgery.

Recent studies have shown that surgical repair of the aortic valve is a good alternative to valve replacement for many forms of AR [27] [4] [28] and avoids many of the complications associated with mechanical and bioprosthetic replacement valves. In children, valve repair has additional advantages including growth potential, delay of valve replacement until the patient is older, and preservation of the pulmonary valve autograft as an option [29]. Good intermediate results have been demonstrated for aortic valve repair of AR due to a

variety of causes [30]. However, aortic valve repair is technically more demanding than valve replacement, and success rates vary among centers [4]. It remains a challenge to expand the successful application of aortic valve repair techniques to a wider patient population.

2.5 Computational modeling of heart valves

2.5.1 Previous computational modeling studies of the mitral valve

Kunzelman et al published the first 3D FE model of the mitral valve in 1993 to study normal valve function [31]. Their model included effects of local fiber direction and assumed linear orthotropic leaflet behavior. A symmetrical, generic leaflet profile from averaged measurements of 4 porcine hearts was used to represent the human mitral valve leaflet shape and a generic, non-branching chordae network was assumed. Their simulations showed that the combination of annulus and papillary muscle contraction improve valve function. Subsequent work by the same group used the model to study the effect of chordal replacement with sutures on valve stress [32, 33]. They also used the model to study the effect of annular dilatation on leaflet stress [34] and to compare two types of annuloplasty ring prostheses to treat the dilation [35]. The model was also applied to support a study on altered leaflet collagen in response to increased leaflet stress [36].

Salgo et al used the FE method to study the effects of annulus shape and leaflet curvature on leaflet stress [37]. They assumed linear orthotropic leaflet behavior and modeled the entire top (atrial) surface of the closed leaflets as a single paraboloid surface. Chordae were neglected entirely.

The group of Redaelli et al in Milan have published a number of FE studies of the mitral valve. One of the first was a FE analysis of the stress on mitral valve leaflets following a valve repair technique in which a point on the free edge of the anterior leaflet is sutured to a point on the free edge of the posterior leaflet to stop regurgitation – the so called edge-to-edge repair [38]. They used a generic, symmetrical leaflet model with linear orthotropic tissue behavior and incorporated only marginal chordae without branching. Another group used the FE method to study leaflet stress in edge-to-edge repair, assuming nonlinear isotropic leaflet behavior [39].

Einstein et al developed a method for implementing a finite strain, hyperelastic strain-energy function for FE analysis of anisotropic membranes [40]. They used this method, along with the geometric leaflet model of Kunzelman, to analyze mitral valve structures and blood flow in simulations that incorporated fluid-structure interaction [41].

In an effort to incorporate more realistic, dynamic boundary conditions, Lim et al tracked points on the mitral annulus and papillary muscles using

sonomicrometry crystals and used these trajectories as dynamic boundary conditions for a FE analysis of the mitral valve over a full cardiac cycle [42]. They modeled the leaflets as a single continuous surface without a distinct anterior or posterior leaflet, and they assumed linear isotropic leaflet behavior and included only marginal chordae.

Prot et al developed a hyperelastic, transversely isotropic membrane shell element and used it in a FE analysis of a very simple geometrical model of the mitral valve [43]. They initially included only 20 marginal chordae but found that they had to add strut chordae to help control leaflet billow. They recently developed a more realistic geometric description of the leaflets and applied the same shell element to analyze the effect of hypertrophic obstructive cardiomyopathy on mitral leaflets stress [44].

Votta et al applied their FE model to compare different mitral annuloplasty prostheses [45]. They further developed this model to incorporate geometry and movement of the mitral annulus and papillary muscles [46].

All of the modeling work discussed so far used generic leaflet profiles, most lacking the multiple lobes of the posterior leaflet. Given the wide variability in human mitral valve leaflet morphology, the use of generic models for patient-specific surgical planning is not appropriate. There have only been two groups who have published computational studies of the mitral valve where valve leaflets

are defined in their entirety from medical imaging. Wenk et al developed a FE model of the LV including the mitral valve, developing a mesh of the mitral valve leaflets directly from segmented MRI images [47]. The chordae, however, could not be seen on the MRI images, so a generic chordae network was assumed. They used a hyperelastic, transversely isotropic model for leaflet tissue behavior. They used the model to study the effect of post-infarct myocardial remodeling on mitral valve competence through papillary muscle displacement. Burlina et al have also presented an image-based approach, segmenting mitral valve leaflets from 3D ultrasound images [48]. They demonstrated the ability to mesh the leaflets in the open state then predict the closed state using simulation. Again, they could not discern chordae in the ultrasound images. They incorporated tethering forces at selected nodes on the leaflet free edge, neglecting the tethering effects of secondary chordae.

All of these published models of the mitral valve make significant simplifications regarding the anatomy of the chordae network. The first simplifying assumption is the use of a generic model of the chordae network. The morphology of both the chordae network and the leaflets varies greatly among individuals [49]. Furthermore the closed state of the leaflets is strongly dependent on the anatomy of the chordae network due to the direct tethering effect of the leaflet by the chordae. It is not clear that using a generic chord model with either a generic or a patient-specific leaflet models will yield simulations with useful predictive power. The second simplifying assumption is the consideration of only

primary chordae. These prior modeling studies incorporate only primary chordae, or primary chordae plus the two strut chords, citing a study that shows that the absence of secondary chordae does not negatively affect leaflet coaptation [11]. However that same study underscores the importance of the secondary chordae by noting the large decrease in cardiac output that results from severing them.

Generic models of the mitral valve present a problem with respect to model validation. There is no way to experimentally validate simulation results because the modeled valve is a theoretical construct. Consequently, validation efforts presented in prior modeling studies have been either indirect or entirely absent. Indirect methods include comparing a physical variable predicted by the valve to levels measured for actual valves. Physical variables used for validation have included tension in a chord, valve closure time, leaflet closing velocity, and heart valve closure sound. Of the two groups to utilize image-based models of the leaflets, only one validated the simulated closed state of the leaflets against the actual position of the closed leaflets measured directly from images [48].

2.5.2 Previous computational modeling studies of the aortic valve

Computational modeling has been used extensively to study the aortic valve. Much of this work has focused on the design of prosthetic tri-leaflet valves with the aim of reducing stresses in the prostheses and improving their longevity. In 1973, Gould et al used the FE method to analyze stress in tri-leaflet valves with the goal of informing the design of prosthetic valve leaflets [50]. Their results

showed that stresses in a leaflet are highly sensitive to its shape. Sabbah used FE simulations to show that porcine bioprosthetic valve leaflet calcification correlated with regions of high stress [51]. Hamid et al used a similar model to study the effect of prosthesis stent height on leaflet stress [52]. Black et al analyzed a bicuspid stented bioprosthesis to assess leaflet stress and the role of bending stress [53]. Krucinski et al studied the effect of rigid versus expanding stents on compressive leaflet stress due to bending [54]. Thornton et al investigated the effect of varying the thickness and stiffness of polypropylene leaflets in prosthetic valve design [55]. Cacciola et al showed that a stentless fiber-reinforced prosthetic valve exhibits a stress reduction of 75% with respect to stented version [56]. Xiong et al used dynamic FE analysis to evaluate several designs of stentless pericardial bioprostheses with single point attached commissures [57].

Modeling studies have used increasingly realistic descriptions of tissue mechanical properties. Sun et al modeled a pericardial bioprosthetic valve under static load using a Fung elastic material model which accounted for the nonlinear anisotropic behavior of the pericardial tissue used to construct leaflets [58]. Kim et al used a similar model in a dynamic analysis in order to investigate leaflet stresses during the opening phase of the valve [59].

In addition to the study of prosthetic valves, computational methods have also been used to study the normal function, disease and repair of native aortic valves.

In 1998, Grande et al published a 3D FE model of the aortic valve basing leaflet and aortic root geometry on human MRI data [60]. They used the model to assess the effect of anatomical asymmetry on stresses in the valve during diastole, showing that leaflet and root asymmetry cause asymmetrical stresses in the leaflets and aortic root. They subsequently extended their model to study the effect of aortic root dilation on valve competence [61]. They also simulated a surgical repair procedure referred to as aortic valve sparing in which the native valve leaflets are sewn into a vascular graft. They used their model to explore the effects of graft shape and stiffness on valve function [62]. Beck et al also used a FE model to study this procedure, showing that aortic root grafts that incorporate the anatomical sinuses result in reduced leaflet stresses [63]. Lim et al studied a repair technique involving replacement of each of the three leaflets with grafts made from pericardium, evaluating the effect of innate curvature of the graft on leaflet stresses and coaptation [64].

Whereas Grande et al assumed linear behavior of leaflet tissues, Li et al showed the importance in using a nonlinear anisotropic leaflet description for prediction of stresses [65]. Gnyaneshwar et al performed dynamic FE analysis of the native aortic valve over a complete cardiac cycle and helped illuminate the dynamic interaction between leaflets and the root [66]. Their study assumed linear elastic leaflet behavior, but Ranga et al used dynamic FE analysis to show the importance of modeling leaflet nonlinearity [67]. Conti et al recently presented a FE model of the aortic valve with aortic root geometry obtained from magnetic

resonance images [68]. They used the model to study the effects of asymmetry of the aortic root on stresses throughout the cardiac cycle.

All of the computational studies presented so far have been purely structural models, neglecting the interaction between tissues and the blood flow. Since 2003, several groups have presented computational studies of the aortic valve to study fluid-structure interaction in the normal aortic valve [69][70][71][72]. Weinberg et al included fluid-structure interaction in multiscale simulations of the aortic valve, describing mechanical behavior at the organ, tissue and cell level [73].

In conclusion, many different methods have been applied to study various aspects of heart valve function, disease and repair. While many of these studies are used to evaluate specific repair strategies like a new annuloplasty ring design or a new repair technique, none of these studies deliver fully image-based models or simulations that run fast enough for intraoperative clinical use.

3 An anisotropic mass-spring model of heart valve tissue: comparison with a finite element model

3.1 Introduction

Surgical repair of heart valves is difficult due to their intricate structure and complex properties; biomechanical studies have shown that leaflets of heart valves exhibit an anisotropic, nonlinear stress-strain relationship and large deformations under physiological loads [10, 31, 74, 75]. Furthermore, repairs are normally performed during open heart surgery when the heart is emptied of blood and the valves are motionless, making it difficult for the surgeon to know how a given surgical modification will translate into valve function after the heart has been closed and blood flow restored. A surgical simulator based on patient-specific medical images has been proposed as a way to improve surgical outcomes [76]. Under the proposed scheme, pre-operative images are acquired, and a computational mesh of the malfunctioning valve is generated. The surgeon explores potential repair strategies on the computer model of the open valve then uses simulation to predict the closed state of the valve. For this surgical planning environment to be of practical use to a surgeon, simulations must be fast – no more than a few minutes per valve closing cycle – so that multiple surgical repair strategies could be simulated in succession, with feedback from one simulated repair guiding the subsequent simulated repair in an iterative process.

Published computational models of heart valves use the finite element (FE) method to study normal, pathological and prosthetic valves and to evaluate innovative devices or methods for surgical repair [31, 39, 42, 46, 65-67, 77-79]. The FE method can provide accurate approximation to the behavior of continua, but FE simulations of heart valves are typically slow due to large deformations, complex constitutive laws, and numerical stiffness of the system equations. While most heart valve FE studies do not report simulation times, a recent FE model of the mitral valve developed for surgical planning reports simulating one closing cycle in 81 hours, and simulation time drops to 7.5 hours using a high performance computing cluster with 32 parallel CPU's [80]. Speed limitations have precluded use of computational models for patient-specific surgical planning and for real-time surgical simulation of heart valves.

Mass-spring (M-S) models have been used to simulate deformable surfaces [81-83], and they can typically be simulated at rates much faster than continuum methods due to their computational simplicity. M-S models can be applied to either structured or unstructured meshes, although only unstructured meshes will be considered here due to their predominance in automatic mesh generation methods. M-S models are fundamentally discrete, and they can be a poor approximation to the underlying continuum [84]. This is especially true of unstructured meshes. Van Gelder has proposed a simple method for choosing spring stiffness to minimize inhomogeneities in deformation due to the mesh [83]. Other groups have proposed optimization methods for tuning individual spring

stiffness throughout a given mesh to approximate specific behavior of the overall surface [85-87]. These methods, however, involve considerable precomputation, which can be problematic for a surgical planning system where the mesh is modified prior to each simulation. In their simplest form, M-S models define an elastic force between two vertices that varies with edge length. However, variants have been proposed to simulate various material properties. For example, Bourguignon et al proposed a M-S method for handling anisotropy by restricting all internal forces to axes aligned with local principal material axes instead of mesh edges [88]. Delingette presented a method for simulating isotropic hyperelastic membranes using a new type of spring, which is based on finite strain mechanics and allows a formal connection between FE and M-S methods [82].

For fast simulation of heart valve closure for use in patient-specific surgical planning, the decision of whether to use M-S or continuum-based methods for modeling the valve leaflets hinges on the relative accuracy and computational cost of these methods. In this study, we assess this tradeoff between speed and accuracy. We present a M-S model that approximates the anisotropic, nonlinear in-plane behavior of aortic valve leaflet tissue on unstructured triangular meshes, and compare the accuracy and computational cost of M-S and FE models. Both models are implemented in the same programming environment so that they can be run on the same input meshes and using the same solvers, allowing us to directly compare computational speed and accuracy. To assess accuracy of the models, we first compared stress-strain curves of simulated square patches of

membrane under biaxial loading to stress-strain curves calculated directly from the constitutive law. We then simulate pressure loading of aortic valve leaflets at end-diastole – both a single leaflet of an aortic valve and a full valve consisting of three leaflets – and we compare critical dimensions of the deformed meshes produced by both the M-S and FE methods. Simulations of biaxial loading illustrate the aspects of material behavior that the M-S model can and cannot accurately capture, while pressure loading simulations help assess model behavior as it is relevant for heart valves.

3.2 Methods

3.2.1 Continuum model for aortic valve leaflet tissue

To simulate the in-plane response, the following Fung-type constitutive law was used to approximate the leaflet response

$$S_{ij} = \frac{\partial W}{\partial E_{ij}} \quad 3.1$$

where S is the second Piola-Kirchhoff stress tensor, E is the Green strain tensor, and i and j are indices representing the two principal directions, and W is the strain energy density. We assume an exponential form for W after Fung [89]

$$W = \frac{c}{2}(e^Q - 1) \quad 3.2$$

where c is a constant and Q represents the following combination of components of the Green strain tensor

$$Q = A_1 E_{11}^2 + A_2 E_{22}^2 + 2A_3 E_{11}E_{22} + A_4 E_{12}^2 + 2A_5 E_{11}E_{12} + 2A_6 E_{22}E_{12} \quad 3.3$$

The values A are constants, and these along with c are determined with a Levenberg-Marquardt nonlinear curve fitting algorithm to the results of previously published biaxial experiments on normal aortic valve leaflet tissue [90].

3.2.2 Computational models of anisotropic membrane

3.2.2.1 Mesh generation

For simulations of biaxial loading, a square patch 15 mm on a side was meshed into a given number of triangles by randomly scattering points within the square then repeatedly connecting the points using Delaunay triangulation and adjusting the positions of all points interior to the boundaries by treating all triangle edges as springs with equal spring constant and resting length and solving for the global equilibrium position of the interior points. This process of triangulating and adjusting the nodes typically converged after 8-10 iterations to a set of nearly equilateral triangles. In order to characterize the variability in simulation results due to mesh discretization, biaxial test simulations were performed on a set of 10 meshes with similar number of triangles (229 +/- 1) and similar mean triangle quality (0.95). Triangle quality is defined as $q = 4a\sqrt{3}/(s_1^2 + s_2^2 + s_3^2)$, where a is the area of the triangle and s_i are the lengths of its three sides [91]. This index equals 1.0 for an equilateral triangle, and $q = 0.6$ is generally considered as a threshold below which numerical approximation and/or stability may suffer, although in practice this threshold is highly problem-dependent.

For simulations of aortic valves, a single leaflet was represented as a semicircle with diameter of 20 mm fixed along its semi-circumference to the inside wall of a cylinder with circumference of 60 mm. Again, a set of 10 semicircular meshes with similar number of triangles (221+/- 2) and similar mesh quality (0.95) was generated and used for simulations of a pressure loaded leaflet. A complete aortic valve model was produced by combining three identical semicircular leaflets arranged circumferentially around the inside wall of the cylinder (Fig. 3.1). Mesh generation used the same method as for the square patch.

3.2.2.2 Equations of motion

Response of the patch to both biaxial and pressure loading was simulated by lumping the mass of each triangle at the nodes then solving for the dynamics of the system of masses. The method used to discretize and solve the equations of motion is described in the Appendix. The FE model and M-S models compared in this study differ only in how they compute the internal forces. The following sections describe the M-S and FE methods for computing these internal forces.

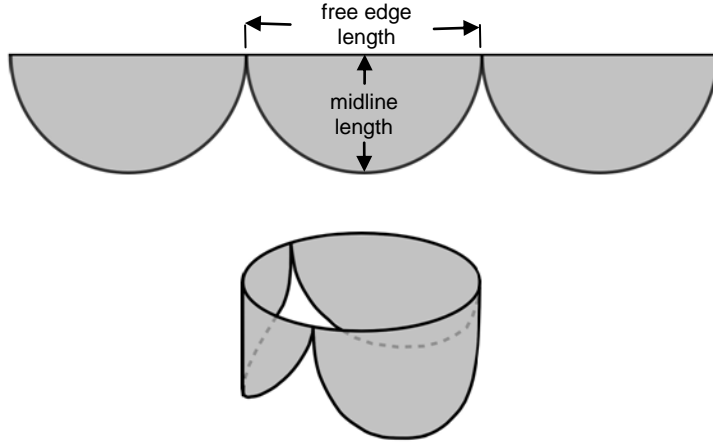


Figure 3.1 A single aortic valve leaflet is represented by a semicircle and a complete aortic valve as 3 semicircles arranged in a row (top sketch) then wrapped into a cylinder (bottom sketch) whose circumference is exactly three semicircle diameters. Each semicircular leaflet is constrained along its semicircumference by virtue of its attachment to the aortic root. The top edge of each leaflet, whose length is equal to the semicircle diameter in the initial, unstressed state of the leaflet, is not attached to the aorta and is referred to as the leaflet free edge. This free edge length and the length of the leaflet midline are defined in the top sketch and are used to describe the degree of deformation of the leaflets. I assumed an unstressed leaflet diameter of 20 mm.

3.2.2.3 Internal forces for mass-spring model

I model an unstructured triangular mesh as an M-S system by treating each triangle edge as a spring (Fig. 3.2). The mass of each triangular element,

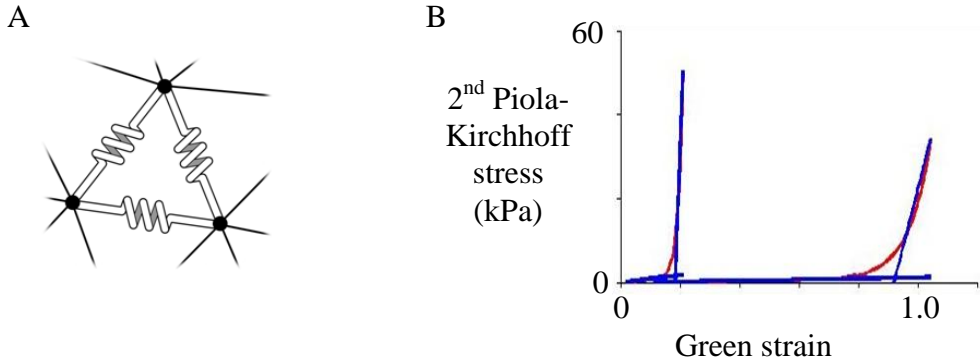


Figure 3.2 (A) Unstructured triangular meshes are treated as mass-spring systems by lumping the triangle mass at its vertices and treating all triangle edges as springs. (B) Spring constants are computed based on leaflet stiffness, which is approximated by a bilinear relationship (blue lines), with parameters determined by best fit to the phenomenological constitutive law (red curves) fit to experimental data.

computed as the product of its area, thickness and density, is distributed equally among its three vertices. The force in each triangle edge (spring) is computed as the product of the magnitude of the deflection of the spring from its resting length, the spring constant, and the unit vector describing the present direction of the edge. We wish to choose spring constants to approximate the nonlinear anisotropic in-plane behavior described by Eqns. 3.1-3.3. Since our goal is simulating heart valves under uniform pressure loading, we make the simplifying assumption that the two stress-strain curves corresponding to equibiaxial loading (one curve for the fiber direction and one for the cross-fiber direction) sufficiently describe the in-plane response. We approximate each of these curves with a piecewise linear fit consisting of a segment of slope m_1 passing through the origin

and a second segment of slope m_2 and intersecting the first segment at some critical value of Green strain, which we express as stretch ratio λ^* . For a given spring at angle ϕ with respect to the material fiber direction, in-plane behavior at some intermediate angle between the fiber and cross-fiber directions is computed by assuming that these piecewise fits vary smoothly with direction ϕ . Specifically,

slope m_1 for example, varies with ϕ according to:

$$m_1(\phi) = \sqrt{m_{1f}^2 \cos^2 \phi + m_{1c}^2 \sin^2 \phi},$$

where m_{1f} is the initial slope in the fiber direction and m_{1c} is the initial slope in the cross-fiber direction. The other parameters, m_2 and λ^* , vary similarly and can be computed for every spring in the mesh based on the angle ϕ in the undeformed state of the mesh. To compute the spring constant for a given spring, we use an equation proposed by van Gelder for calculating spring constants throughout an unstructured triangular mesh in order to control membrane behavior [83]

$$k_c = \frac{Eh \sum_i \text{area}(T_i)}{|c|^2} \quad 3.4$$

where k_c is the spring constant for edge c of a given triangle, E is Young's modulus for the leaflet tissue, h is leaflet thickness which is assumed uniform and equal to 0.5 mm, the summation term represents the area of all triangles sharing edge c , and the denominator is the squared length of edge c . In place of Young's modulus, E , we use the slope m_1 or m_2 , depending on whether the present deformation of the spring corresponds to a value of stretch less than or greater than λ^* .

Two spring constants for each spring, one for small and one for large displacements, are pre-computed at the start of a simulation as is the stretch ratio, λ^* , at which each spring undergoes its change in stiffness. During the simulation, the force in a given spring is computed as

$$\vec{f} = k_1(l - l_0)\hat{n} \quad 3.5$$

for springs with stretch magnitude less than λ^* and as

$$\vec{f} = (k_1 l_0 (\lambda^* - 1) + k_2 (l - \lambda^* l_0))\hat{n} \quad 3.6$$

for springs with stretch magnitude greater than λ^* . In these equations, k_1 and k_2 are spring constants for the low and high stiffness regimes of the spring, respectively, l is the present length of the spring, l_0 is the rest length of the spring and n is the unit vector describing the present direction of the spring. The force in the spring is then applied to the two nodes bounding it, and the net internal force on each node in the mesh is computed by summing the contributions of all springs sharing a given node.

3.2.2.4 Internal forces for finite element model

In order to evaluate the computational cost of a finite element model of an anisotropic membrane as well as to have a reference to which to compare accuracy of the M-S model simulations, a FE model formulated for large deformations and unstructured triangular meshes was implemented. We use a model presented by Taylor et al. that was derived directly from membrane assumptions rather than by simplifying shell theory [92]. This results in a conceptually and computationally straightforward formulation. The basic

equations are reproduced here, but the reader is referred to the cited source for a more thorough presentation.

The Green strain tensor for a given triangular element in the mesh can be computed as

$$E = 0.5(C - I) \quad 3.7$$

where I is the 2×2 identity matrix and C is the right Cauchy-Green deformation tensor, computed as $C = G^T g G$. Here, G and g are J^I and j^{-I} , respectively, where J and j are the Jacobian matrices mapping the position of a point in global coordinates to the parametric representation adopted within a triangle, referred to the initial and current reference frame, respectively. Specifically,

$$g = \begin{pmatrix} (\Delta x^{21})^T \cdot \Delta x^{21} & (\Delta x^{21})^T \cdot \Delta x^{31} \\ (\Delta x^{21})^T \cdot \Delta x^{31} & (\Delta x^{31})^T \cdot \Delta x^{31} \end{pmatrix} \quad 3.8$$

where Δx^{21} is the vector from vertex 1 to vertex 2 of the triangle in its present (deformed) configuration, and, similarly, Δx^{31} is the vector from vertex 1 to vertex 3. Matrix G is given by

$$G = \begin{pmatrix} \frac{1}{|\Delta X^{21}|} & \frac{-(\Delta x^{21})^T \cdot \Delta X^{31}}{|\Delta X^{21}| |V_3|} \\ 0 & \frac{|\Delta X^{21}|}{|V_3|} \end{pmatrix} \quad 3.9$$

where ΔX^{21} is the vector from vertex 1 to vertex 2 of the triangle in its original (undeformed) configuration, and, similarly, ΔX^{31} is the vector from vertex 1 to vertex 3. Vector V_3 is defined as the cross product of ΔX^{21} and ΔX^{31} .

The Green strain tensor computed using Eq. 3.7 describes strain relative to the local (triangle) coordinate system which, because of the unstructured nature of the triangle mesh, is arbitrarily oriented with respect to the global coordinate system. This tensor must be rotated to the principal axes of the tissue in order to apply the constitutive law in Eqns. 3.1-3.3. This is done using

$$E' = R \begin{pmatrix} E_{11} \\ E_{22} \\ E_{12} \end{pmatrix} \quad 3.10$$

where E_{ij} is the i,j^{th} component of the Green strain tensor and R is the strain transformation matrix given by

$$R = \begin{pmatrix} \cos^2\theta & \sin^2\theta & -2\sin\theta\cos\theta \\ \sin^2\theta & \cos^2\theta & 2\sin\theta\cos\theta \\ \sin\theta\cos\theta & -\sin\theta\cos\theta & \cos^2\theta - \sin^2\theta \end{pmatrix} \quad 3.11$$

where θ is the angle between side ΔX^{21} of the triangle and the local fiber direction of the material measured in the original configuration of the mesh. Now the 2nd Piola-Kirchhoff stress tensor with respect to the principal axes of the tissue, S' , is computed using the constitutive law given in Eqns. 3.1-3.3, and is then rotated back to the local reference frame using the inverse of transformation matrix R . Components of the local stress tensor, S , are then used to compute the forces on the nodes of the triangle due to internal forces as

$$f = -AHB^T \begin{pmatrix} S_{11} \\ S_{22} \\ S_{12} \end{pmatrix} \quad 3.12$$

where A and H are the area and thickness of the triangle in its original configuration, and B is defined by

$$B=Qb \quad 3.13$$

where Q is the stress transformation matrix, expressed in terms of the elements of G in Eq. 3.9 as

$$Q = \begin{pmatrix} G_{11}^2 & 0 & 0 \\ G_{12}^2 & G_{22}^2 & G_{12}G_{22} \\ 2G_{11}G_{12} & 0 & G_{11}G_{22} \end{pmatrix} \quad 3.14$$

and b is the 3x9 strain displacement matrix given as

$$b = \begin{pmatrix} -(\Delta x^{21})^T & (\Delta x^{21})^T & (0 \ 0 \ 0) \\ -(\Delta x^{31})^T & (0 \ 0 \ 0) & (\Delta x^{31})^T \\ -(\Delta x^{21} + \Delta x^{31})^T & (\Delta x^{31})^T & (\Delta x^{21})^T \end{pmatrix} \quad 3.15$$

Thus, the 9 elements of f from Eq. 3.12 are the three components of the force on vertex 1, followed by those on vertices 2 and 3. The nodal force contributions from all triangles in the mesh are summed to get the net internal forces on nodes throughout the mesh.

3.2.2.5 External forces for biaxial loading

Biaxial loading was simulated by applying external forces consisting of in-plane tensile loads distributed along edges of the square patch and aligned perpendicular to the edge upon which they act with respect to the initial state of the mesh. Five states of biaxial stress were simulated corresponding to ratios of peak Lagrangian stress in one test axis to that in the other (perpendicular) axis of 20:60, 30:60, 60:60, 60:30, and 60:20 kPa. A biaxial loading protocol was simulated by applying forces to the edges of the patch to maintain a constant ratio of Lagrangian stress between the two test axes. Simulations were performed for fiber direction both coincident with one of the test axes and at 45° to it.

Since the system is dynamic, simulating a given loading curve involves running a dynamic simulation at a series of incremental steps in applied stress and waiting until a steady-state is reached at each step. For all simulated loading curves, we used increments of 0.025, 0.050, 0.1, 0.2, 0.4, 0.7, and 1.0 times the peak stress for that loading condition. Damping forces sufficient to critically damp all nodes in the mesh were added to each node in order to produce fast, stable simulations.

To determine the strain undergone by the deformed mesh, four virtual markers in the shape of a square, 1.5 mm on a side, were located in the center of the patch. Sides of the square were aligned with the fiber direction. For the undeformed state of the mesh, the location of each marker was computed in barycentric coordinates relative to the three vertices of the triangle containing it. During deformation, the positions of the markers were used to compute the components of Green strain. A given loading increment is determined to have converged when changes in both normal strains of the marker array become small (less than 2% of cumulative strain for that loading increment). The value of Lagrangian stress for that loading increment was converted to 2nd Piola-Kirchhoff stress, which, along with the value of Green strain from the marker array, was used to describe the constitutive behavior of the mesh as it is deformed.

3.2.2.6 External forces for pressure loading

Pressure loading of the aortic valve mesh was simulated by applying a constant, surface normal pressure of 80 mmHg to all mesh triangles. Resulting nodal loads were applied to the aortic surface of mesh triangles, i.e., in the direction corresponding to radially inward (toward the axis of the cylinder) in the undeformed state of the mesh. All three semicircular leaflets are constrained by fixing all mesh vertices that lie on the semi-circumferences. Simulations are terminated when the incremental displacement of the middle of a leaflet free edge becomes small (below 10^{-5} mm).

3.2.2.7 Solution method

The method used for discretizing and solving the system of equations is not critical to the aim of this study. I chose to discretize the equations using a second-order backward difference method with semi-implicit numerical integration as described in the Appendix. Adaptive time step control based on step-doubling was incorporated [93]. A conjugate gradient method was used to solve the sparse linear system [94]. Computation was implemented in the Matlab programming language (Mathworks, Natick, MA).

3.3 Results

A set of 7 parameters describing the in-plane response of aortic valve leaflet tissue was generated by curve fits to experimental stress-strain data (Table 3.1).

Table 3.1 Parameters of aortic valve leaflet constitutive law computed by fitting data from biaxial testing experiments.

Parameter	Value
c	9.7 Pa
A ₁	49.558
A ₂	5.2871
A ₃	-3.124
A ₄	16.031
A ₅	-0.004
A ₆	-0.02

Deformation of a square patch using the FE model was simulated for five states of biaxial stress corresponding to ratios of Lagrangian stress in the x- to y-directions of 20:60, 30:60, 60:60, 60:30 and 60:20 kPa (Fig. 3). The final deformed states of the mesh are shown for the case where the material fiber direction coincides with P_x (Fig. 3.3, middle row) and where the material fiber direction is oriented at 45° to P_x in the undeformed configuration (Fig. 3.3, bottom row).

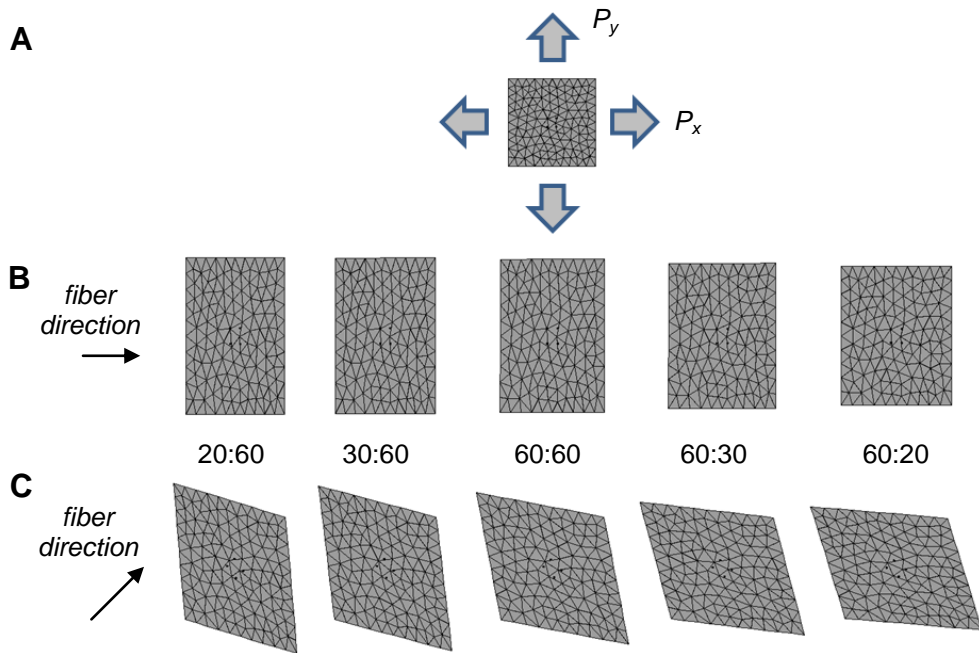


Figure 3.3 Simulated deformation of a square patch of membrane under biaxial load. (A) Undefomed mesh showing directions of applied stresses, (B) Deformed mesh under the 5 states of biaxial stress ($P_x:P_y$) = 20:60, 30:60, 60:60, 60:30, 60:20 kPa, where the material fiber direction coincides with the x-axis, (C) Deformed mesh under the same 5 states of stress but with the material fiber direction in the undeformed state oriented at 45° to the x-axis. All deformed meshes in this figure were produced using FE simulations.

Plots of stress versus strain were generated for the FE simulations (Fig. 3.4). For equibiaxial loading and normal strains (Fig. 3.4, middle row, columns 1 and 2), the mean error magnitude in strain for the FE simulations with respect to the actual constitutive law for the final loading increment is 0.004%. For non-

equibiaxial loading states and normal strains (Fig. 3.4, rows 1, 2, 4 and 5, columns 1 and 2), the mean error magnitude in strain is 0.9%. For shear strains (Fig. 3.4, column 3), the mean error magnitude in strain is 3.1%. Note that for all of the stress vs. strain plots for the FE simulations (Fig. 3.4), the standard deviations are so small that the gray region is very narrow and appears as a single curve.

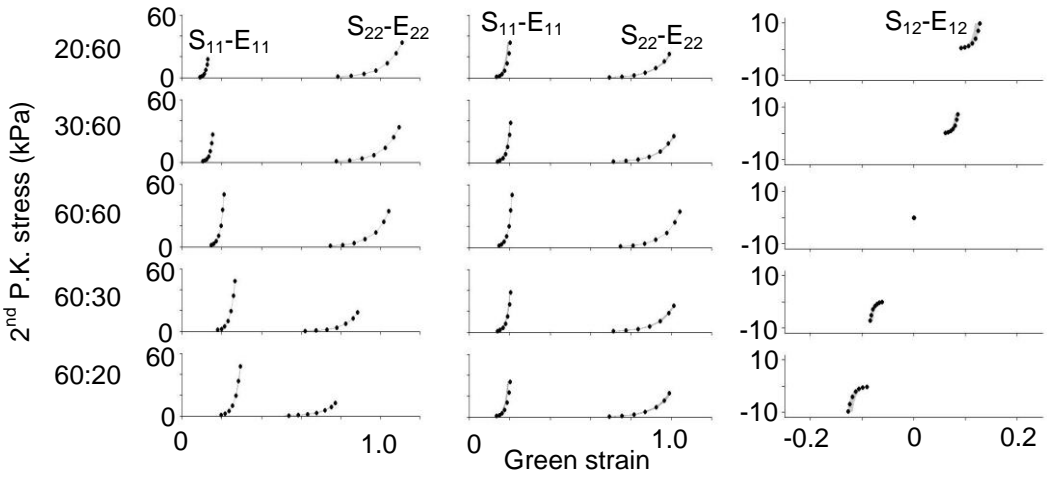


Figure 3.4 Stress-strain curves for FE model. Second Piola-Kirchhoff stress in the fiber direction (S_{11}) and cross-fiber direction (S_{22}) is plotted as a function of Green strain for five biaxial loading curves. Loading states, determined by the ratio of peak Lagrangian stress in the x -direction to that in the y -direction, are, from top to bottom, 20:60, 30:60, 60:60, 60:30, and 60:20 kPa. The left column of plots shows normal stress vs. strain for the case where fiber direction coincides with the x -axis. The middle and right columns of plots show normal stress vs. strain and shear stress vs. strain for the case where the fiber direction is at 45° to the x -axis. The solid black circles represent the stress-stretch relationship calculated directly from the 7-parameter constitutive law. The gray curves represent the relationship computed from simulations and demarcate the mean strain \pm one standard deviation at each of the stress increments across the 10 test meshes.

Plots of stress vs. strain were generated for the M-S simulations (Fig. 3.5). For equibiaxial loading and normal strains (Fig. 3.5, middle row, columns 1 and 2), the mean error magnitude in strain for the M-S simulations with respect to the actual constitutive law for the final loading increment is 1.7%. For non-equibiaxial loading states and normal strains (Fig. 3.5, rows 1, 2, 4 and 5, columns 1 and 2), the mean error magnitude in strain is 7%. For shear strains (Fig. 3.5, column 3), the mean error magnitude in strain is 81%.

Pressure loading of a single aortic valve leaflet was simulated using the FE and M-S models and the final deformed state of the mesh was plotted for each (Fig. 3.6A and 3.6B). Two important metrics of leaflet deformation, free edge length and radial midline length, were computed for the deformed meshes and compared (Table 3.2). Differences in absolute position of the nodes of the two meshes were computed and mapped onto the nodes of the original (flattened) leaflet (Fig. 3.6C). Mean and maximum magnitudes of the difference in nodal position were 0.4 and 0.9 mm, respectively.

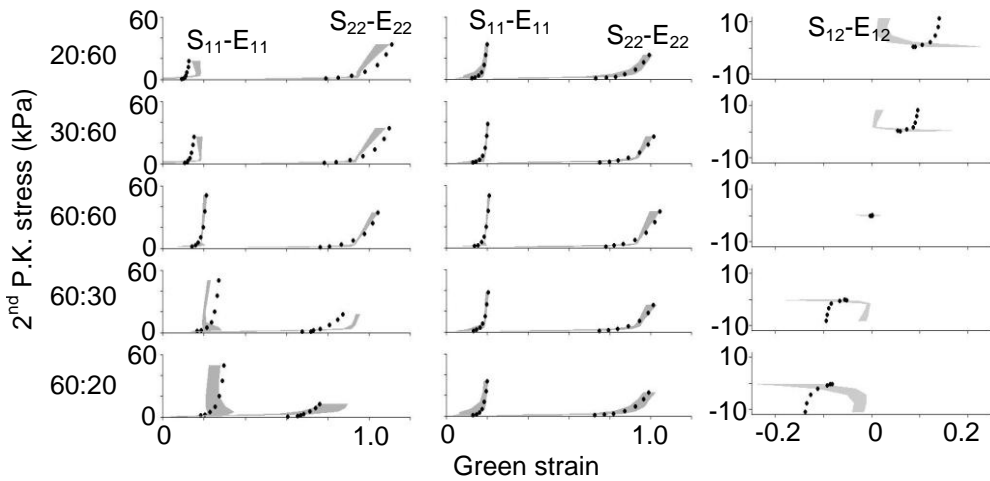


Figure 3.5 Stress-strain curves for the mass-spring (M-S) model. Second Piola-Kirchhoff stress in the fiber direction (S_{11}) and cross-fiber direction (S_{22}) is plotted as a function of Green strain for five biaxial loading curves. Loading states, determined by the ratio of peak Lagrangian stress in the x -direction to that in the y -direction, are, from top to bottom, 20:60, 30:60, 60:60, 60:30, and 60:20 kPa. The left column of plots shows normal stress vs. strain for the case where the fiber direction coincides with the x -axis. The middle and right columns show normal stress vs. strain and shear stress vs. strain for the case where the fiber direction is at 45° to the x -axis. The black solid circles represent the stress-strain relationship calculated directly from the 7-parameter constitutive law. The gray curves represent the relationship computed from simulations and demarcate the mean strain \pm one standard deviation at each of the stress increments across the 10 test meshes.

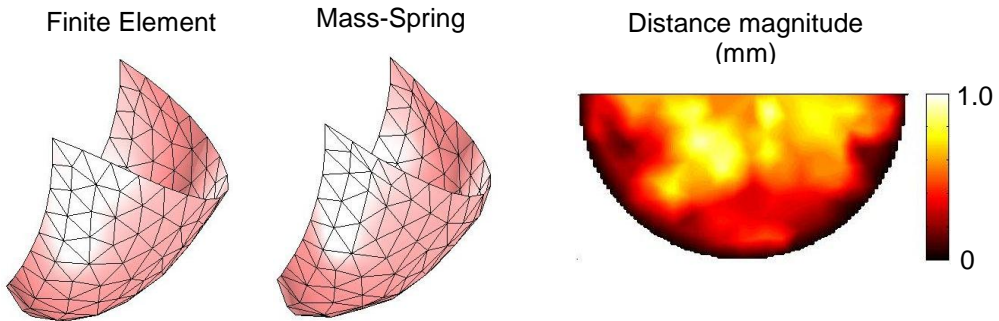


Figure 3.6 The final deformed states of a simulated aortic valve leaflet subject to a static pressure load of 80 mmHg. The semicircular mesh is constrained along its semi-circumference. Images, from left to right, show the deformed leaflet simulated with the FE model, the deformed mesh simulated with the M-S model, and the discrepancy between the two deformed meshes expressed as the magnitude of the distance between corresponding nodes on the models and mapped onto the undeformed mesh.

Pressure loading of a 3-leaflet aortic valve was simulated using the FE and M-S models, and the final deformed state of the mesh was plotted for each (Fig. 3.7A-D). The most clinically useful feature of the loaded valve is the extent of coaptation (i.e., overlap) between adjacent leaflets. We determine this for the two models shown by computing the distance between each mesh node and the nearest point on the surface of adjacent leaflets. Because repulsive contact forces are used to handle self-collisions of leaflets, a non-zero gap of approximately 0 to 1.5 mm exists between leaflets that are in contact. The shape of the coaptation (contact) zone is estimated as the region enclosed by the contour line

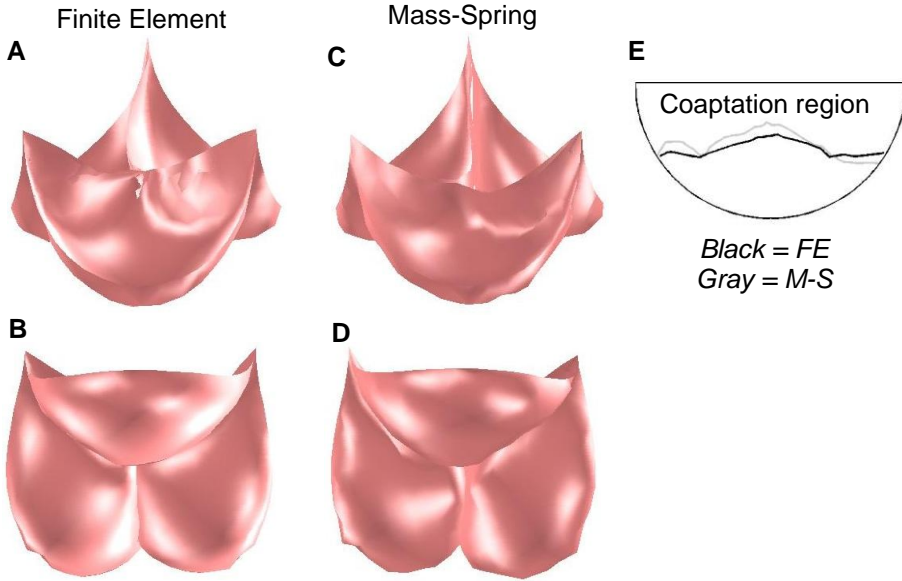


Figure 3.7 The final deformed state of a simulated aortic valve (3 leaflets) subject to a static pressure load of 80 mmHg. Top oblique and bottom oblique views of the final deformed state of the mesh produced by the FE model are shown in panels A and B, respectively. The same views are shown for the M-S model in panels C and D. Panel E shows the coaptation region computed from the closed valve meshes for both models. The coaptation region is the portion of the semicircle bounded by the free edge on top and the irregular curve on the bottom.

corresponding to an inter-leaflet distance of 1.5 mm (Fig. 3.7E). Maximum principal stress along with shear strain was plotted for the FE simulations of the full valve (Fig 3.8, panel A).

Table 3.2 Comparison of dimensions of the deformed valve leaflet meshes predicted by the finite element (FE) and mass-spring (M-S) methods.

	Free edge length (mm) mean \pm SD	Radial midline length (mm) mean \pm SD
Undeformed Mesh	20.0	10.0
Mass-Spring	26.3 ± 0.2	15.2 ± 0.3
Finite Element	26.20 ± 0.02	15.60 ± 0.04

The computational cost of the two methods for computing internal forces was assessed in two ways. The first method involved counting the number of operations required to compute internal forces on the nodes of one triangle during one time step of the model. (Computation of all other components of the simulation was the same for the M-S and FE methods.) Operations were classified as multiplications (including divisions), additions (including subtractions), assignments, or other (e.g., square roots, inequalities, decisions, transcendental functions). The total number of floating point operations (FLOPs) was calculated by counting all operations as one FLOP except for square roots and transcendental functions, which were counted as 10 FLOPs each (Table 3.3). The second method involves measuring the actual time spent executing the portion of the program that performed these computations of internal forces. Execution time was then normalized by dividing by the execution time for the FE model (Table 3.3).

Table 3.3 Comparison of the computational cost of the finite element (FE) and mass-spring (M-S) models for computing internal forces. Operation counts and computation time are given per element per one time step of the dynamic simulation.

Method	X, ÷	+, -	Assign	Other	FLOPs	Time re: FEM (%)
FEM	187	148	114	3	479	(100)
M-S	13	15	9	1	51	10

3.4 Discussion

The goal of this study was to develop an efficient M-S model that could simulate highly anisotropic membranes – about five times more distensible in one principal direction than in the other–on unstructured triangle meshes. Central to the development of this model was quantification of model speed and accuracy in order to assess its suitability for simulating heart valves as part of a surgical planning system. The M-S method examined here is faster but less accurate than the simple FE model with which we compared it. However, the M-S model does reasonably well at approximating the deformation of a pressurized aortic valve with complex biomechanical properties, with simulated positions of leaflet nodes lying within 0.9 mm of nodal positions predicted by FE. Results of simulated biaxial loading illustrate the aspects of material behavior that the M-S model can and cannot accurately capture, while pressure loading simulations quantify accuracy as it is relevant for simulating a heart valve.

For the parameters listed in Table 3.1, the direct plots of the constitutive law for loading in the fiber direction (Fig. 3.4, left column, solid black circles) show that the stress-strain curves for the fiber direction move to the right as the applied stress increases in the fiber direction and decreases in the cross-fiber direction. The FE model incorporates the constitutive law directly and thus captures this behavior accurately (Fig. 3.4, left column, gray regions). Interestingly, dependence of the stress-strain curves on the overall state of stress is observed in the M-S model (Fig. 3.5, left column, gray regions), although curves are not as close to the analytical solution as for the FE model, and variation due to the particular mesh discretization is greater. This dependence on the overall state of stress is probably due to the fact that the behavior in the two principal directions is entangled in the edge spring model as a result of the nearly continuous distribution of orientations of springs; forces in most of the edge springs have components in both principal directions.

Plots of the constitutive law also show that the relationship between normal stress and strain is almost independent of shear strain (Fig. 3.4, middle column, solid black circles), as evidenced by the fact that all of the curves in the column are similar, despite a large positive shear strain in the top panel and large negative shear strain in the bottom panel. This follows from the constitutive law parameters A_5 and A_6 being very close to zero. Constitutive law plots also show that the shear stress vs. strain relationship exhibits an exponential form similar to that for the normal stress strain relationship (Fig. 3.4, right column, solid black

circles). The M-S model does a poor job of approximating shear stress (Fig. 3.5, third column). This is not surprising because our simple M-S model includes no shear springs and thus does not allow direct control of shear behavior. However, the state of loading of an actual heart valve leaflet under pressure load approximates equiaxial stress in regions far from constraints. To estimate the degree and distribution of shear strain in a loaded aortic valve, we computed shear strain at each node on the pressurized leaflet mesh deformed using the FE model and plotted the value at the location of the node in the undeformed (flattened) leaflet (Fig. 3.8, panel B). The majority of the leaflet mesh exhibits shear strain of less than 0.1 (shear angle of approximately 6°), with the maximum value of 0.27 (shear angle of approximately 15°) occurring near the points of attachment of the leaflet free edge to the cylinder (aorta) wall.

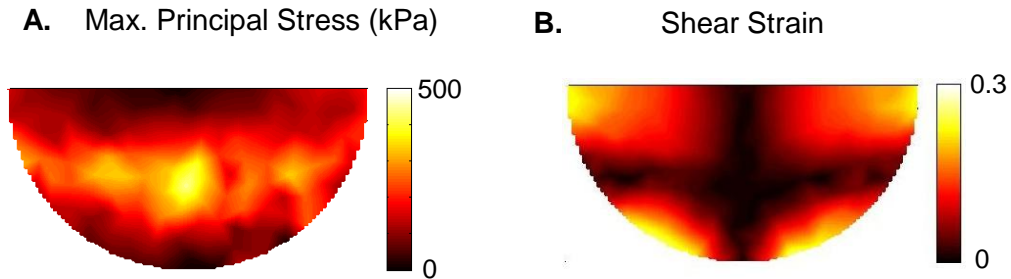


Figure 3.8 (A) Maximum principal stress (kPa) in one leaflet of the pressure-loaded valve deformed by the FE model. (B) Magnitude of shear strain (Green strain) throughout the mesh of the pressure-loaded leaflet deformed using the FE model.

Results of simulated pressure loading of the single leaflet model show that the overall shape of the deformed M-S mesh is very similar to that of the deformed FE mesh (Fig. 3.6, A and B). The most salient differences are the overall smoothness of the FE mesh compared to the M-S mesh and the greater shear deformation in the M-S mesh near the constrained termini of the free edge. A consequence of this exaggerated shear is that the free edge is in a slightly lower position than in the FE mesh. This lower free edge combined with a slight bulging of the M-S mesh in the region just below the free edge results in the maximum discrepancy in nodal position of almost 1 mm (Fig. 3.6C). The computed length of the free edge of the deformed mesh is almost identical in the FE and M-S models, while the length of the radial midline is underestimated in the M-S model re: FE (Table 3.2). This reflects slightly decreased distension in the M-S model in the cross-fiber direction and is also seen in the biaxial loading results (Fig. 3.5, right column, middle panel).

The FE simulations of the full aortic valve under pressure exhibit similar leaflet shape, and similar leaflet stress pattern and magnitude, to published studies [95] [66] [60]. M-S model simulations show very similar closed valve shape to the FE models. Again leaflet surfaces are somewhat smoother in the FE than the M-S model, and in-plane shear deformation appears to be larger in the M-S model near the points where the free edges are constrained (Fig. 3.7, panels A-D). As in the single leaflet model, this causes the free edges of the three leaflets in the M-S model to drop to a lower position than in the FE model. The lower boundary of

the coaptation region is similar for the M-S and FE models, although it is somewhat “noisier” for the M-S model. The region predicted by the M-S model is somewhat narrow and is probably a manifestation of the position of the free edge due to the overestimation of in-plane shear strain in the M-S model.

Based both on counts of floating point operations and on compute times, the M-S model is about ten times faster than the FE model, a figure which agrees with published observations regarding speed comparison between M-S and FE methods [83, 96]. Our method of counting operations is approximate and neglects important computing details. For example the number of clock cycles to compute a floating point addition is not typically the same as for division, and the cost of “other” (e.g., trigonometric) functions can vary with choice of algorithm used to implement it. However, the relative proportion of the different categories of operations is similar between methods, so this relatively simple comparison should be valid. Likewise, the values for compute time depend on software and hardware factors, but a bias favoring one method is not apparent. It is important to note that the speed advantage to the M-S model is based only on the steps to compute nodal forces due to deformation. If implicit methods are used to solve the equations of motion, Jacobian matrices must be computed for estimating future values of the nodal forces. The simplicity of the spring model formulations makes the computation of the Jacobians considerably simpler too, and it is likely that this would lead to further speed advantages for the M-S method. In fact, for the semi-implicit integration methods used for this study, the M-S model was

typically 20 to 30 times faster than the FE model. However, we were unable to express the computational difference as a straightforward FLOP comparison due to the nature of the iterative conjugate gradient solution method and to the different time step histories produced by the M-S and FE simulation.

It is difficult to determine a maximum value of acceptable error for simulations in the context of a surgical planning system for heart valves. Valve repair surgery is not currently based on a quantitative approach that relates intraoperative valve dimensions to quantitative outcome measures of repair success. Errors due to the M-S modeling method of less than 1 mm seem small compared to overall valve dimensions, and are also a fraction of the coaptation height (overlap) characterizing normal valve closure. Still, many factors independent of the modeling method introduce uncertainty into patient-specific models, including mesh geometry and properties of the valve tissue (e.g., material fiber direction and constitutive behavior, both of which exhibit significant spatial variability within a given valve as well as between individuals). Any computational system used for surgical planning would have to undergo thorough validation to ensure accurate predictive value prior to clinical use.

The M-S and FE models compared here are membrane formulations and are only valid for structures in which bending stiffness is much smaller than in-plane stiffness. However, this study is concerned with predicting the configuration of the closed valve at peak load when the leaflets are operating in the regime where

in-plane stresses are relatively large - at least an order of magnitude greater than bending stresses [97, 98]. Another limitation concerns the use of bilinear models to approximate the constitutive law. These are valid only for the range of stresses used to compute parameters of the bilinear fit. For example, the exponential constitutive law presented here would predict continuing increases in membrane stiffness as stress increases above 50 kPa, but the bilinear functions maintain constant stiffness at these higher stresses. However, the constitutive law itself is not valid above that stress level, as it was produced by fits to experimental data over a similar range of stresses as used here. Another important limitation of the M-S model is the absence of control of resistance to shear deformation. However, due to the way that heart valves are loaded and constrained, response to shear only appears to be important in limited regions close to point-constraints. Thus it is possible to avoid the computational burden of modeling shear behavior explicitly without paying a high price in terms of accuracy. In cases where the M-S model is used to predict deformation of valves following surgical modification, consequences of neglecting shear behavior could become more serious for cases where the repair results in valve anatomy or shear properties that differ significantly from that of a normal valve.

The anisotropic, nonlinear M-S model described here has been shown to simulate aortic valve leaflets under pressure load at considerable speed-ups with respect to an efficient FE membrane model and with only minor difference in the deformed state of the mesh. This difference in simulation time could enable a

practical surgical planning system using present computing power. M-S systems lend themselves to being solved on parallel architectures because of the local nature of the forces between nodes [84], and several groups have developed methods for solving M-S systems on the GPU [99-101]. The computational advantages of M-S models combined with the speed-up of parallel computing may enable real-time surgical simulation of anisotropic heart valves in the near future.

4 Finite element model of aortic valve surgical repair using grafted pericardium

4.1 Introduction

Aortic valve repair often involves leaflet reconstruction, and a common repair strategy is to graft a new leaflet created from the patient's own pericardium into the valve [102]. However, native valve leaflet tissue and treated pericardium exhibit different mechanical properties, and our clinical experience has shown it to be difficult to determine the size of the pericardial graft that will form an adequate seal with the remaining native leaflets when the valve is closed and loaded.

Computational models of the aortic valve have been used to study both normal [60, 66, 67, 69, 70, 103] and diseased [61] valves and to evaluate bioprosthetic [57, 58, 77, 104] valves. They have also been used to study valve repairs, including aortic root replacement with synthetic grafts [62] and replacement of all three aortic valve leaflets with fixed pericardium [64].

We use a structural finite element (FE) model of the aortic valve to explore the effect of pericardial leaflet graft size on the closed, loaded state of the repaired valve. Leaflets are described by anisotropic, hyperelastic constitutive laws, and we model all three leaflets in their entirety and resolve leaflet collisions in order to simulate repair strategies that are asymmetrical with respect to valve geometry

and leaflet properties. We use the model to explore surgical repair strategies by simulating valve closure for a range of sizes of the pericardial autograft.

4.2 Methods

4.2.1 Computational mesh of aortic valve

We create a computational mesh of an aortic valve by meshing a planar leaflet then joining three such leaflets and wrapping them into a cylinder. Leaflet shape is taken from published studies [105-107]. The curve describing the lower edge of an excised leaflet lying flat (i.e., the edge that attaches to the aortic root not including the commissures) takes the form: $y=\sin^2(x)/\tan(\gamma)$ where γ is 22° after [106]. Variables x and y are in normalized units relative to the diameter of the base of the aortic root, and the width of the leaflet is 1.047 in normalized units. In absolute dimensions, we chose the diameter of the base of the aortic root to be 20 mm, and we use a commissure height of 5 mm based on clinical observations (Fig. 4.1).

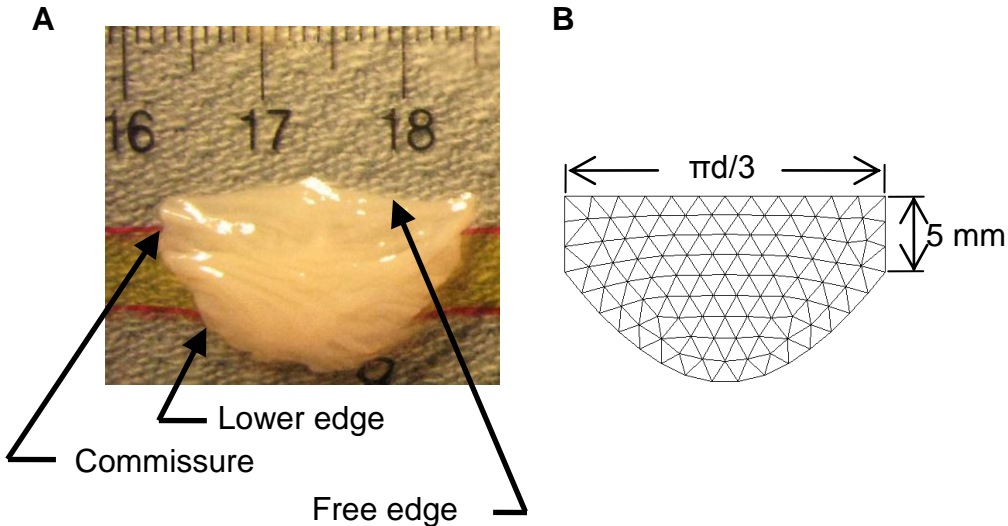


Figure 4.1 The aortic valve leaflet. (A) Photograph of a fresh excised porcine aortic valve leaflet. (B) Mesh of unstructured triangles in the shape of a single aortic valve leaflet. Leaflet width is given in terms of d , the diameter of the cylinder formed by joining three such leaflets at their commissures and “wrapping” them onto a cylinder.

A planar leaflet is meshed into a given number of triangles by randomly scattering points on the leaflet, connecting the points using Delaunay triangulation, then moving interior points in order to equalize triangle side lengths. Equalization is done by treating all triangle edges as springs, with equal spring constant and rest length, and solving for the global equilibrium position of the interior points. Triangulation and equalization are repeated until the mesh converges to a set of nearly equilateral triangles. Mesh uniformity is quantified by computing the average quality of all triangles. To quantify triangle quality, we use a common index [91]: $q = 4a\sqrt{3}/(s_1^2 + s_2^2 + s_3^2)$, where a is the area of the triangle and s_i are the lengths of its three sides. Quality equals 1.0 for an

equilateral triangle, and values below approximately 0.6 are often associated with diminished accuracy and/or stability for FE analysis. An example of a meshed leaflet used in this study has mean quality of 0.97, with range of 0.78 to 1.0 (Fig 4.1B).

The lower edges of the valve leaflets, along with the edges at the commissures, are attached to the aortic root, and the locus of points defining this attachment has been shown to lie on a cylinder [105, 106]. Accordingly, we create a three-leaflet valve model by joining three planar leaflets at the commissures and wrapping them into a cylinder (Fig. 4.2A). We will refer to the diameter of this cylinder as the diameter of the aortic root, ignoring the sinuses that bulge from the aortic root behind each leaflet. In this cylindrical mesh, the leaflets are in the unstressed state, but the cylinder diameter does not necessarily correspond to the unstressed state of the aortic root, i.e., when trans-aortic pressure is zero. In fact, the sum of the lengths of the leaflet free edges is known to be greater than the circumference of the unstressed aortic root (Fig. 4.3). Published data [103], corroborated by our images of pressurized porcine aortas, show the sum of the leaflet free edges to be approximately 15% greater than this circumference. Thus, we compute the diameter of the root at zero pressure as 20 mm/1.15.

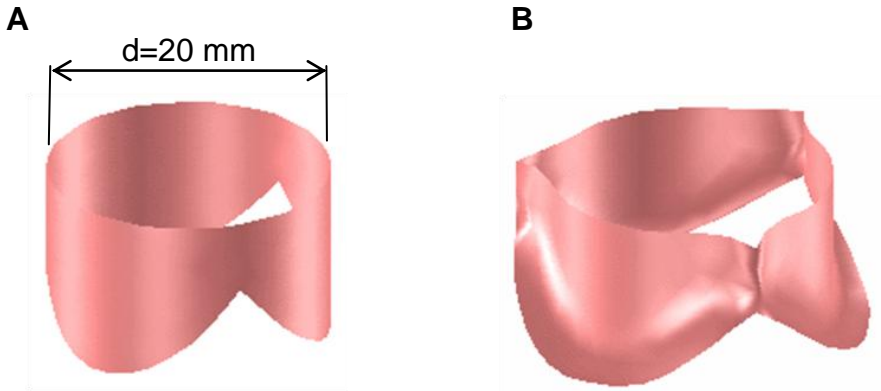


Figure 4.2 Geometry of the aortic valve model. (A) Three leaflets joined at the commissures and wrapped into a cylinder. (B) Three-leaflet mesh deformed by dilating the cylinder to which the constrained edges (lower edges and commissures) of the leaflets are attached.

I simulate aortic valve loading in two steps, first distending the aortic root to its diameter at 80 mmHg then fixing the nodes where the leaflets attach to the aortic root and loading the leaflets with 80 mmHg of pressure. Since I am only interested in the static final loaded state of the valve and I do not consider fluid flow in the sinuses, I effectively treat the aortic root as a boundary condition for the leaflets. Rather than meshing the entire aortic root, which would more than double the size of the mesh and greatly increase computation time, I distend the aortic root by treating it as an elastic tube with wall thickness and Young's modulus taken from published data [60]. To every boundary node I attach a spring, connected to and perpendicular with the cylinder axis. Spring constants are computed by equating the spring force with the force due to wall stress in the

elastic tube for the portion of the tube corresponding to that boundary node. Then, to determine the positions of the boundary nodes at the start of leaflet pressurization, equilibrium is found between boundary node forces due to trans-aortic pressure, those due to the springs representing the elastic aortic root, and any forces due to leaflet tension that act on the boundary nodes (Fig. 4.2B).

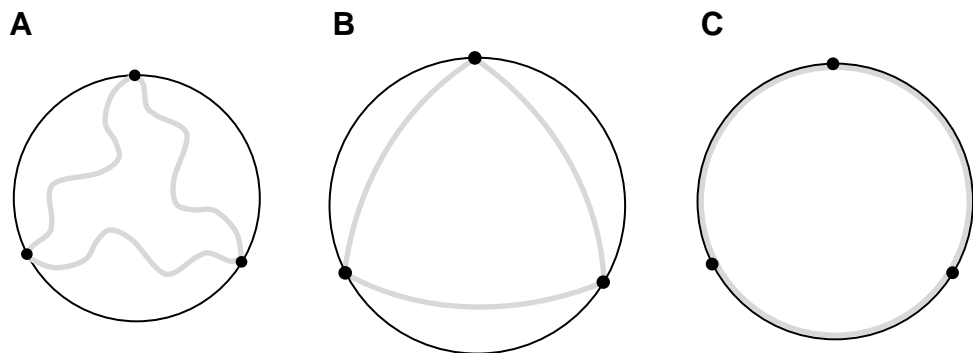


Figure 4.3 Relationship between the unstressed leaflet free edges and the aortic root diameter for different levels of aortic pressure. Aortic valve leaflet free edges are shown in gray, and the cylinder describing the attachment of the leaflets to the aortic root is shown as a thin black circle. Commissure points are shown as black dots. (A) At aortic root pressure of zero (atmospheric), the sum of the lengths of the leaflet free edges is greater than the circumference of the aortic root. (B) At aortic root pressure of 80 mmHg, the sum of the lengths of the leaflet free edges (unstressed) is less than the circumference of the aortic root. (C) For some intermediate value of aortic root pressure, the sum of the leaflet free edges exactly equals the circumference of the aortic root.

4.2.2 Finite element simulation

Deformation of the mesh subject to uniform pressure loading is simulated and a static solution for the final deformed state of the valve is sought. While this is ostensibly a quasi-static analysis, this approach is problematic due to the large displacements undergone by portions of the mesh, including complex buckling and self-collision, while undergoing almost no change in strain energy. For this reason, I simulate the structure dynamically. The mass of the triangular elements is lumped at the nodes then the dynamics of the system of masses is simulated using the method described in the Appendix. Pressure loading is simulated by applying a constant pressure of 80 mmHg to all mesh triangles on their aortic surface. Simulations are terminated when the incremental displacement of the middle of a leaflet free edge becomes small (below 10^{-5} mm).

4.2.3 Contact handling

Complex intra-leaflet folds and inter-leaflet contact can arise as the leaflets close, so mesh-wide collision detection must be deployed continually during the simulation, requiring substantial computation. We implemented an efficient, two-step contact handling strategy. First, the large number of possible triangle pair collisions is dramatically reduced by maintaining a sorted list of axis-aligned bounding boxes of all triangles [108]. This allows us to check a relatively small number of triangle pairs that have overlapping bounding boxes for direct triangle to triangle intersection. If a node of one triangle is found to lie less than some

distance, d , in front of the other triangle surface, a contact force is applied to that node in the direction of the triangle surface. The magnitude of the contact force is

$$f_{contact} = \begin{cases} |f_{ext}| e^{-kd/|f_{ext}|}, & d \geq 0 \\ |f_{ext}| - kd, & d < 0 \end{cases} \quad 4.5$$

where f_{ext} is the net external force acting on the node, d is the perpendicular distance between the node and the face of the triangle (with positive values of d lying on the side toward which the surface normal vector points), and k is the contact stiffness. Using this method, the reaction force on the node due to contact with the triangle balances the component of the external force (due to pressure) driving the node toward the triangle. This prevents interpenetration of colliding leaflets and produces frictionless contact. The contact force vanishes quickly outside the collision zone then transitions smoothly to a linear penalty force for interpenetration, avoiding the high numerical stiffness that would result if the exponential relationship were extended to negative values of d . For the simulations presented here, we used $k=10$ N/m and a collision zone width of 0.1 mm.

4.2.4 Solution method

The semi-implicit numerical integration method used to solve the equations of motion (Appendix) incorporates adaptive time-step control based on step doubling [93], using a target truncation error of 1.0e-5 meters. The method of stabilized biconjugate gradients [94] is used to solve the sparse linear system. Computation is implemented in the Matlab programming language (Mathworks,

Natick, MA), with computational bottlenecks, such as collision checking and computing Jacobian matrices for implicit integration, written in C.

4.2.5 Analysis of valve closure

Effective closure of the aortic valve requires that the leaflets completely obstruct the aorta to prevent retrograde flow. In addition, there must be considerable overlap between adjacent closed leaflets during normal heart beats if the valve is to still close completely during periods of high diastolic pressure (e.g., exercise). A normal aortic valve exhibits significant overlap (coaptation) at the valve center during normal heart beats. To compute the portion of the leaflets involved in coaptation, the region of contact is computed between adjacent leaflets by ray casting from one leaflet, finding the distance to the nearest intersecting triangle on neighboring leaflets, then computing the region of the leaflet over which this distance is less than some threshold. I chose this distance to be 0.5 mm – equal to leaflet thickness in my model.

4.3 Results

Simulations of the normal aortic valve, consisting of three identical leaflets with dimensions and properties of native valve leaflets, produced a symmetrical closed valve (Fig. 4.4A-B). The coaptation region of each leaflet is approximately bounded by the free edge, the two commissures, and lines from the bottom of the commissures to a point along the leaflet midline that lies approximately 3 mm

below the free edge (Fig. 4.4C). Simulations were run with pericardial leaflet grafts of varying width (0%, 7%, 14%, 21% and 27% greater than the native leaflet width) and height (0%, 13%, 27% and 40% greater than the native leaflet height). Results for two of these cases are shown (Fig. 4.4D-I).

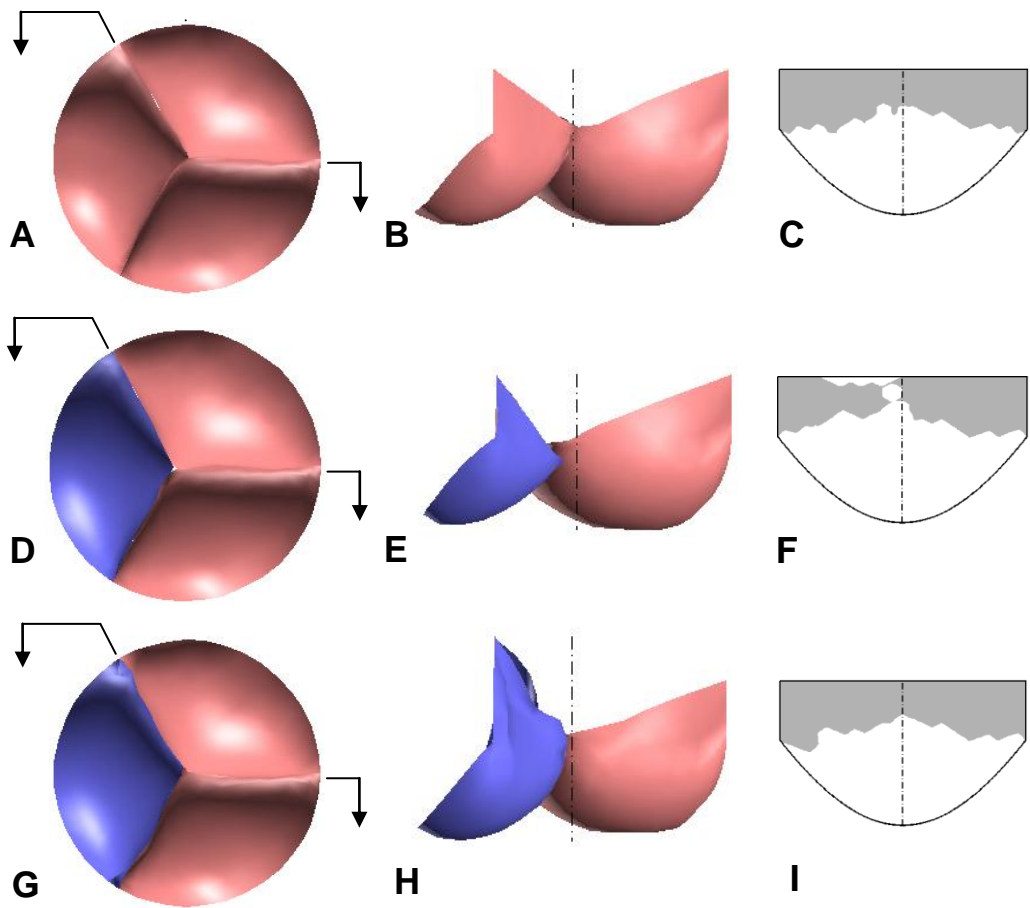


Figure 4.4 Results of finite element simulations of aortic valve closure.

(A-C) Bottom view, side view with one leaflet cut away, and coaptation region for simulation of a normal valve loaded with 80 mmHg of pressure, representing peak diastolic pressure in the aorta. (D-F) Same images as above but with one normal leaflet replaced with a pericardial graft (shown in blue) of the same height but 7% wider than the native leaflet. (G-I) Same images but for graft that is 27% higher and 21% wider than the native leaflet.

For each combination of leaflet width and height, the coaptation map for one of the native leaflets was analyzed to estimate the minimum coaptation height, and results are presented in graph form (Fig. 4.5). For pericardial leaflet graft height equal to that of the native leaflet, simulations show that coaptation is small or incomplete for all graft widths (Fig. 4.5, first point on horizontal axis). Similarly, for pericardial leaflet graft width equal to that of the native leaflet, coaptation is small (< 1 mm) for all graft heights (Fig. 4.5, solid dark blue line). As both leaflet width and height increase, minimum coaptation height increases, reaching a maximum of 3 mm for grafts 27% higher than native leaflets.

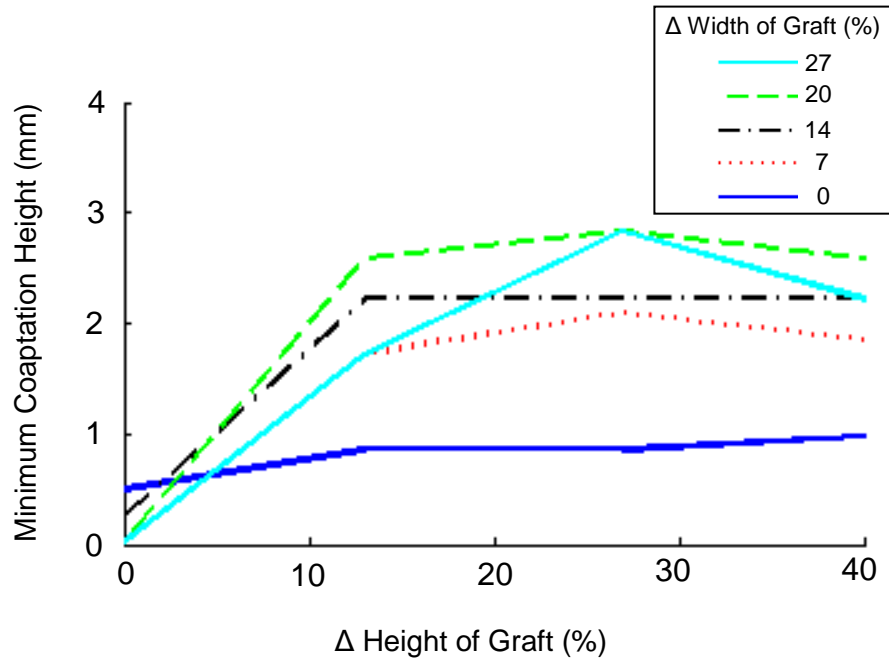


Figure 4.5 Effect of pericardial leaflet graft width and height on leaflet coaptation. Graft dimensions are expressed in percent increase relative to the width and height of the native leaflet.

4.4 Discussion

The primary goal of this study was to use a FE model of aortic valve leaflets to inform the repair of the aortic valve using autologous pericardium. Simulating leaflet grafts in a range of widths and heights showed that the differences in properties of pericardium and native valve leaflets necessitate that the pericardial leaflet width and height both be greater than those of the native leaflets in order to achieve adequate coaptation. Furthermore, simulations reveal a complex relationship between graft size and effectiveness of the repair. If graft height is not increased, the leaflet is not able to reach the coapting surfaces of the native leaflets and instead slides under them for increasing graft widths. This leads to a central gap in the simulated closed valve corresponding to a central regurgitant jet in an actual valve. This finding agrees with clinical observations at Children's Hospital, Boston. Increases in graft height, in the absence of increases in width, result in a graft that is too tightly constrained due to inadequate length and high stiffness along the width dimension. As leaflet width and height are increased together, coaptation improves, but there is a point beyond which further increases in width cause coaptation to worsen. Because of the increased height, the graft is supported at points higher on the commissures than are the native leaflets, resulting in a larger axial (and smaller radial) component its tethering force. This causes the excess graft material to slide downward past the coaptation surfaces

and allows the native leaflets to extend beyond the center of the valve, reducing their minimum overlap with each other.

The finite element method has been used to predict the effect of pericardial graft shape on aortic valve function [64]. That study, however, neglected the nonlinear anisotropic behavior of valve tissue and only simulated replacement of all three leaflets with identical grafts, limiting the applicability of their results to axially symmetrical valve repairs. The methods presented in this study allow the extension of predictive modeling to the clinically important case of single leaflet replacement and to image based simulations of real valves, where valves are, in general, asymmetrical with respect to the sizes and shapes of the three leaflets.

My simulations of the closed state of a normal valve depend on the in-plane behavior of the leaflet tissue, and tissue properties vary considerably among individuals. To study this effect, I replaced the constitutive law parameters for the native leaflet tissue with those used in another study [103] that result in greater leaflet distensibility in both the fiber and cross-fiber directions. I found that I had to also increase the distensibility of the aortic root to produce normal coaptation, but using the resulting valve to simulate pericardial graft sizing produced plots of minimum coaptation height versus graft height and width that showed similar trends.

Simulations of the normal aortic valve (three native leaflets) suggested that the overall pattern of fiber arrangement throughout the leaflet may play a previously unrecognized role in normal valve function. The pattern of fiber arrangement in a native leaflet was initially chosen to be parallel to the free edge of the leaflet as is typically assumed in computation modeling studies of the aortic valve where orthotropic leaflet behavior is considered. However, using this pattern of fiber arrangement, simulations of the closed state exhibited poor coaptation and downward billowing of the leaflet belly compared to experimental observations and CT scans of normal porcine aortic valves under physiologic pressures. Closer inspection of isolated porcine aortic valve leaflets revealed large visible bundles of fibers that on average run at an angle of approximately 25° to the free edge. Published data collected using small angle light scattering reported a similar collagen fiber arrangement [10]. After incorporating this fiber arrangement into the model of the native leaflet, simulations of the closed valve reproduced several key features of the normal loaded valve including a lack of billowing of the leaflet belly toward the left ventricle and a more realistic shape of the leaflets where they coapt in the center of the valve (Fig. 4.7).

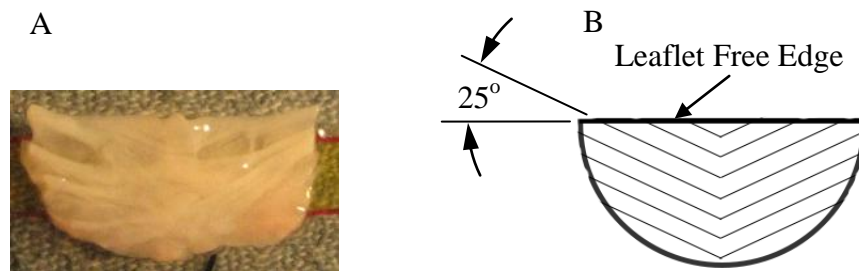


Figure 4.6 (A) Single leaflet of porcine aortic valve floating on a thin layer of phosphate buffered saline in order to observe its unstressed state. (B) Preferential fiber direction is approximated as 25° to the free edge in a pattern that is symmetric about the leaflet midline.

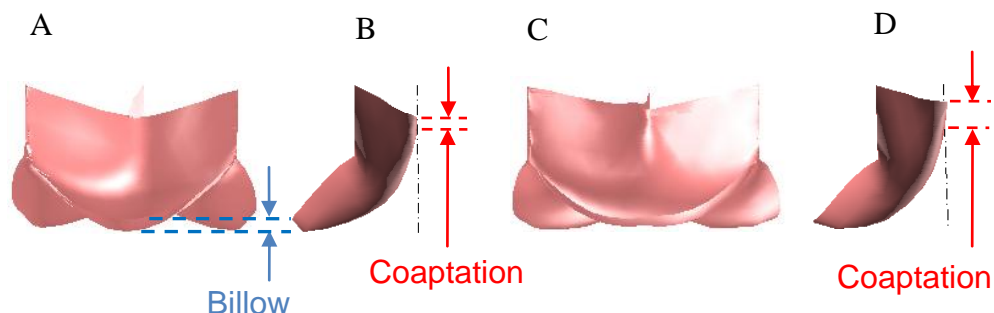


Figure 4.7 (A) Side view looking into one leaflet of closed aortic valve model produced by simulation in which fiber direction was assumed to be parallel to the leaflet free edge. (B) Side view of single leaflet from same simulation, with other two leaflets cut away. (C) Side view looking into one leaflet of closed aortic valve model produced by simulation in which fiber direction is approximated as 25° to the leaflet free edge. (D) Side view of single leaflet from same simulation, with other two leaflets cut away.

I model the native leaflets and pericardium as membranes, assuming negligible flexural stiffness. This is supported by data showing bending stresses at least an order of magnitude smaller than in-plane stresses [97, 98]. I have not assessed the validity of the membrane assumption for diseased leaflets, which are often thickened and calcified. In order to study general design principles involved in constructing pericardial grafts, I have simulated a generic aortic valve design. However, the human aortic valve can be anatomically asymmetrical, with considerable variability between individuals. A patient-specific approach using a medical image based model of the valve should result in a more detailed and accurate surgical planning tool. My simulator has been designed to read in unstructured triangular meshes of all three leaflets, so it can easily be adapted to image-based, patient-specific valve simulation. Future plans include application of these modeling methods to patient-specific models of AR.

5 Image based mass-spring model of the mitral valve

5.1 Introduction

Surgical repair of the mitral valve, like the aortic valve, is technically challenging. A major reason for this is that the valve structures have complex geometry and material properties, making it difficult for the surgeon to predict how the valve leaflets will displace and deform in response to a given repair strategy. A computer-based surgical planning simulator could facilitate valve repair surgery, but such a system has not been realized. The primary factors preventing current mitral valve modeling methods from being used for clinical surgical planning are prohibitively slow computation times and the use of generic models of leaflets and/or chordae geometry. Generic models have been largely used due to the difficulty of deriving patient-specific mitral valve geometry from medical images and the difficulty importing complex image-based valve geometry into commercial software programs for computational analysis.

Using a generic model of valve geometry for planning mitral valve repair for a particular patient carries the obvious disadvantage that the patient's valve might differ significantly from the generic model. The use of generic models also presents a problem for validating simulation results. A patient-specific model can be validated by simulating normal valve closure then directly comparing the simulated closed state with an image of that individual's valve in the closed state.

A generic model, on the other hand, is a theoretical construct, making it impossible to use direct, image-based validation.

Slow computation presents a significant limitation to present computational models of the mitral valve. For intra-operative use, simulations must be able to predict valve function for potential repair strategies quickly so as not to prolong the time that the patient is on cardiopulmonary bypass. The time constraint on computation time is not as strict for pre-operative surgical planning, but there is a limit to how much time a busy surgeon can sit at a computer iteratively running simulations to test potential repair strategies.

In this chapter, I present a fully image-based model of the mitral valve and use it, along with the anisotropic M-S method presented in Chapter 3, to simulate the closed state of the valve under end-systolic pressure. I use this model to explore the effect of secondary chordae on simulation results and to quantify sensitivity of simulation results to parameters describing model geometry and mechanical properties. Finally, I simulate a simple surgical modification – replacing a chord with a suture and varying its length – and assess the accuracy of simulated results.

5.2 Methods

5.2.1 Strategy for creating and validating image-based model

A clinical system for building patient-specific models and simulating various surgical repair strategies was described in Chapter 1 (Fig. 1.1), and the simulation tools presented in this chapter are designed for such a workflow. However, in order to acquire carefully controlled datasets that could be used to validate simulations, a slightly more complicated workflow was used (Fig. 5.1). Valves were imaged in the open position with the resulting image used to create a mesh of the open valve. The mesh of the open valve was used in simulation to produce a mesh of the closed valve. For validation, the same heart was also imaged with the valve in the closed, loaded position, and the resulting image was used to create a mesh of the closed valve. The mesh of the closed valve predicted by simulation could then be directly compared with the mesh created directly from the image of the closed valve.

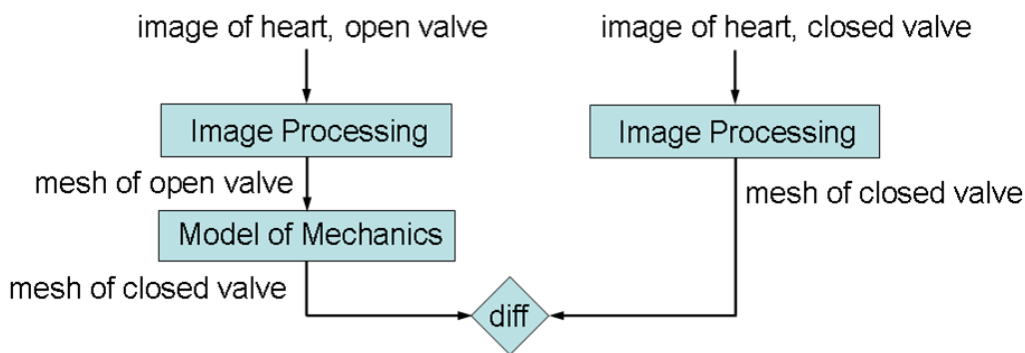


Figure 5.1 Developing and validating an image-based model of the mitral valve.

5.2.2 Simulated closure of normal valves

Three hearts were explanted from 30-40 kg female Yorkshire pigs and stored in phosphate-buffered saline. They were imaged within 24 hours using high resolution computed tomography (MicroCAT, Siemens, Munich, Germany). Low pressure regulators (T-91, 0-5 psi, Marsh Bellofram, Newell, WV) and pressure sensors (ASCX05DN, Honeywell, Freeport, IL) were used to statically load the mitral valve with air at precisely controlled pressures via tubing inserted through the aorta. Hearts were scanned with applied left ventricular pressures of 0 and 120 mmHg (normal peak systolic pressure), producing grayscale volumetric images with isotropic voxel size of 100 μm (Fig 5.2).

Images were cropped, segmented and triangulated using custom written software in Matlab (Mathworks, Natick, MA). The mesh produced from the open valve was used to define the leaflet surface for simulating valve closure (Fig 5.3). I used custom written meshing tools to reduce the total number of triangles in the mesh to 600 – 700. In order to reduce the number of triangles while preserving high triangle quality, edges were collapsed to maintain approximately six edges per node, and edges were treated as springs with equal rest lengths throughout the remeshing.

The open valve mesh was also used to define chordae, specified as the segment endpoints, where each endpoint is either a node on the mesh, a point of attachment to a papillary muscle or a point at which chordae branch. The mesh

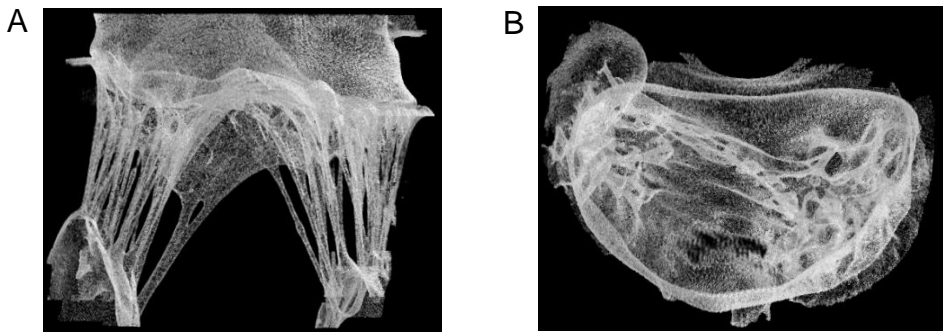


Figure 5.2 Volume rendering of a micro-CT scan of valve 3 under 120 mmHg of pressure, shown from (A) side view and (B) top view.

produced from the pressurized valve (Fig. 5.4) was used to define the closed surface of the pressurized valve to be used for comparison with simulations of the pressurized valve. It was also used to define the annulus and papillary muscle locations to be used as boundary conditions for the simulated closure as well as to define details of the chordae network not revealed by the image of the open valve.

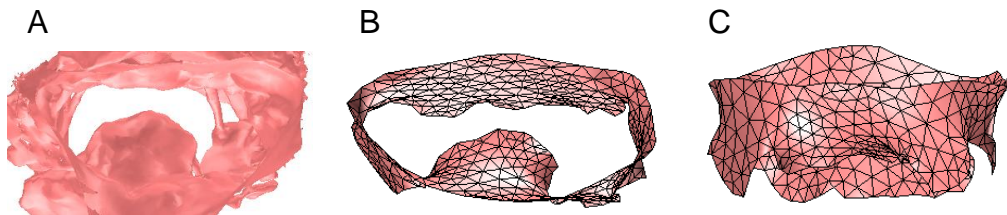


Figure 5.3 (A) Surface rendering of a mesh produced from a micro-CT scan of valve 3 in the open state shown from top view. (B) Mesh from panel A after remeshing and keeping only triangle on atrial surface of leaflets. (C) Mesh from panel B shown from side view.

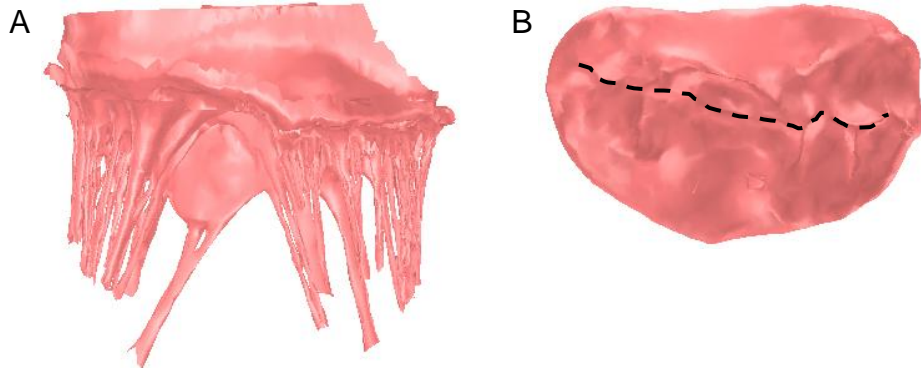


Figure 5.4 Surface rendering of a mesh produced from a micro-CT scan of valve 3 under 120 mmHg of pressure shown from (A) side view and (B) top view with dashed line showing coaptation.

Closure of the mitral valve mesh was simulated using the dynamic M-S model described in Chapter 3. The nonlinear anisotropic behavior of the mitral valve leaflets was modeled using bilinear functions (Fig. 5.5) that approximate published stress-strain data for mitral valve leaflet tissue [75] [10]. Specifically, the Fung exponential constitutive law described in Eqns. 3.1 – 3.2 was also used for the mitral valve with the following parameter choices: $c=9$ Pa, $A_1=80$, $A_2=23$, $A_3=-3$, $A_4=16$, $A_5=0$, $A_6=0$. One bilinear function is used for the preferential fiber direction, generally corresponding to the circumferential direction in the leaflet, and the other is for the cross-fiber direction, referred to as the radial direction in the leaflet. Chordae are modeled as linear elastic rods with constant diameter supporting tension only, with Young's modulus taken from published data [31] (Table 5.1).

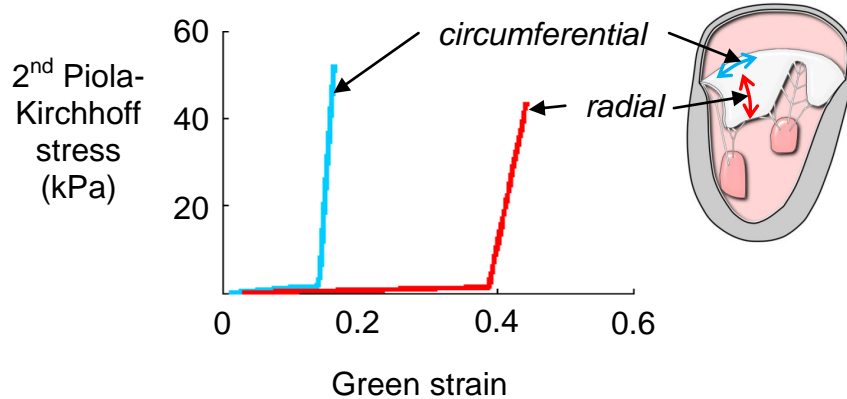


Figure 5.5 Bilinear relationships used to approximate the nonlinear anisotropic behavior of mitral valve leaflet tissue. The circumferential direction is the principal fiber direction and runs parallel to the annulus. The radial direction is perpendicular to the circumferential direction.

Table 5.1 Model parameters used in simulations. Variables are: E =Young's modulus, λ =stretch ratio, ρ =mass density, T =thickness, D =diameter, P_{ES} =end-systolic pressure.

Model Parameter	Value
$E_{\text{fiber direction, pre-transition}}$	0.011 MPa
$E_{\text{fiber direction, post-transition}}$	2.3 MPa
$\lambda_{\text{critical, fiber direction}}$	1.13
$E_{\text{cross-fiber direction, pre-transition}}$	0.0033 MPa
$E_{\text{cross-fiber direction, post-transition}}$	0.76 MPa
$\lambda_{\text{critical, cross-fiber direction}}$	1.33
ρ_{leaflet}	1060 kg/m ³
T_{leaflet}	0.001 m
E_{chord}	40 MPa
D_{chord}	0.0005 m
P_{ES}	16 kPa

Simulation consists of two parts. First, mesh nodes lying on the valve annulus are moved from their positions defined by the open mesh to those defined by the closed mesh, and the positions of the remaining mesh nodes are computed by solving the system state equation subject to displacement boundary conditions on the annulus nodes [109]. Next, mesh dynamics were simulated by applying surface normal forces to the ventricular surface of all mesh triangles corresponding to the applied left ventricular pressure. Semi-implicit numerical integration with adaptive time step control was described in Chapter 3, and contact handling was discussed in Chapter 4. Simulations proceeded until the mesh converged to its final closed state.

5.2.3 Simulated closure of valve following chord replacement and shortening

One of the three valves used for simulation of normal valve closure was used to simulate a simple surgical intervention in which a single primary chord on the posterior leaflet was transected and replaced with size 0 monofilament suture. The suture was tied to the leaflet at the original point of attachment of the transected chord then brought through the papillary muscle and LV wall so that its length could be easily varied. While applying 120 mmHg of air pressure to the LV, the chord was pulled (shortened) as far as possible without causing a leak, then a CT scan of the heart was taken and subsequently meshed (Fig 5.6). This chord shortening procedure was simulated by changing the resting length of the corresponding primary chord on the posterior leaflet of the open valve mesh and simulating valve closure.

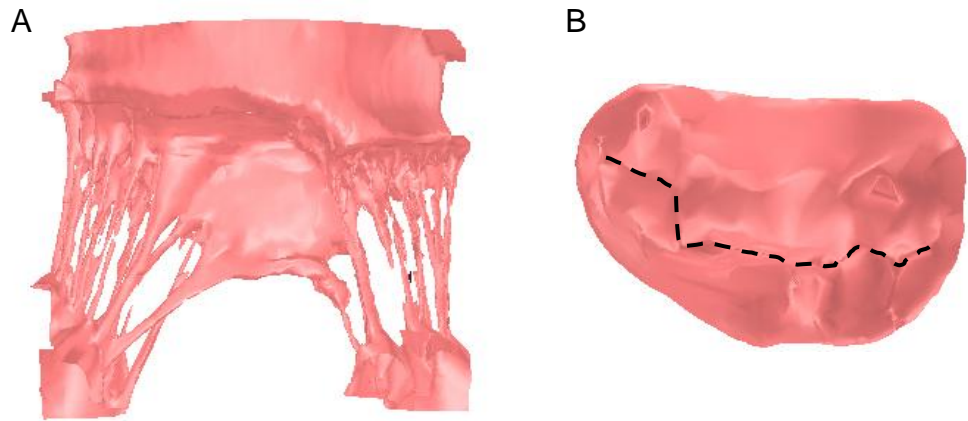


Figure 5.6 Surface rendering of a mesh produced from a micro-CT scan of valve 3 under 120 mmHg of pressure and with one posterior leaflet chord replaced with a length of suture. Mesh is shown from (A) side view and (B) top view, with dashed line showing coaptation.

5.2.4 Image-based validation of simulations

The closed valve meshes produced by simulation were compared with the meshes produced directly from images of the closed valve by registering and overlaying the mesh produced by simulation with the atrial surface of the mesh produced directly from the CT scan of the closed valve. Registration was done using the iterative closest point method using the points of the meshes lying on the boundary at the annulus. Meshes are compared by computing the distance from each node on the simulated closed mesh to the nearest node on the mesh from the image of the closed valve. The maximum in-plane distance from a point on the simulated mesh to one on the mesh from the image is less than 0.5 mm.

5.3 Results

5.3.1 Closed leaflet shape

Valve closure and loading was simulated in less than 25 seconds for each of the three valves, and image based validation resulted in mean surface-to-surface error of approximately 0.8 mm for all three valves (Table 5.2). The maximum surface-to-surface error was 2.4 to 3.0 mm and typically occurred near the line of coaptation as seen in the error maps (Fig. 5.7). When simulations were repeated with all secondary chordae omitted, mean and maximum surface-to-surface errors increased more than two-fold for all three valve models (Table 5.2, last column). Error maps showed that the maximum surface-to-surface error typically occurred in the belly of the anterior leaflet (Fig. 5.8), reaching values of approximately 7 mm.

Simulations in which the posterior leaflet primary chord was replaced and shortened resulted in restricted movement of the portion of the posterior leaflet to which the chord attached. This was visualized by superimposing the simulated closed meshes produced before and after the chord length change, then using cut-planes to examine the resulting change in closed leaflet position (Fig. 5.9, A). The

Table 5.2 Number of triangles, nodes and chord segments comprising the three valve models, along with the simulation time and mean and maximum errors in the closed state for simulations with all chords and with primary chords only. Error is computed as distance from the simulated closed mesh to the mesh produced directly from the image of the closed valve.

valve I.D.	# of triangles	# of nodes	# of chords	time (sec)	e_{all} (mm) mean, max	e_{pri} (mm) mean, max
1	655	414	52	21.4	0.8, 2.4	1.9, 7.4
2	621	406	53	20.0	0.8, 3.0	2.0, 7.2
3	624	425	77	24.8	0.8, 2.5	1.8, 6.4

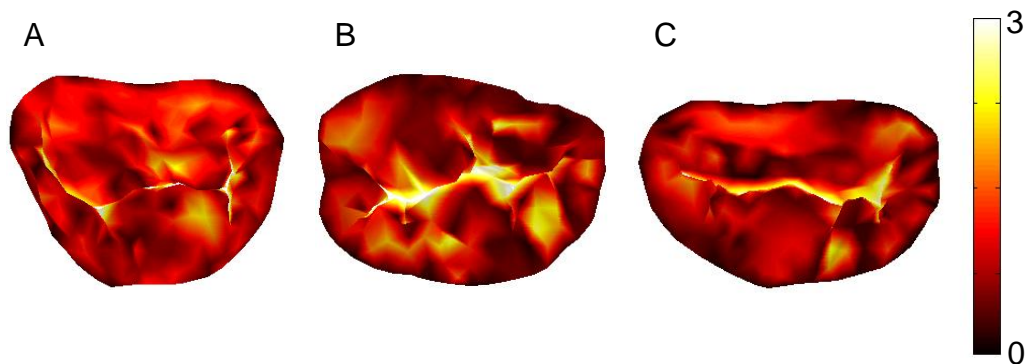


Figure 5.7 Magnitude of error (distance in mm) between closed valve surface predicted by simulation and closed valve surface from image, for valves 1 – 3 are shown in panels (A) – (C), respectively. Simulations were run with all (primary and secondary) chordae.

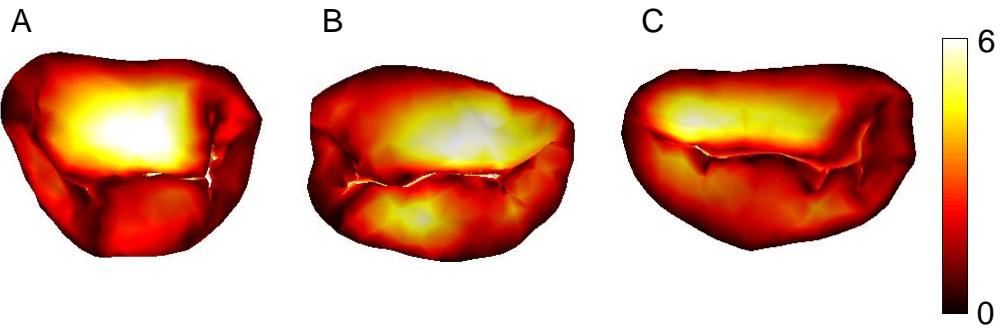


Figure 5.8 Magnitude of error (distance in mm) between closed valve surface predicted by simulation and closed valve surface from image, for valves 1 – 3 are shown in panels (A) – (C), respectively. Simulations were run with primary chordae only. Note change of scale compared to Fig. 5.7.

same was done for the closed meshed produced directly from the CT image before and after actual chord shortening (Fig. 5.9, B). The effect of chord shortening in simulation was to pull the posterior leaflet region in the middle of the valve downward toward the apex of the heart (Fig. 5.9, A, cut-plane 3). This shifted the coaptation to the right, toward the posterior leaflet. This closely mimicked the effect seen in the experimental results (Fig. 5.9, B, cut-plane 8). The change in position of the posterior leaflet shifted the coaptation line toward the posterior leaflet as seen in the top view of the simulated closed valve (Fig. 5.10, A) compared to the simulation prior to chord shortening (Fig. 5.7, C). Again the meshes produced directly from the images of the chord shortening experiment also show a posterior shift in coaptation line in the case with the shortened chord (Fig. 5.6, B) compared to the case prior to chord shortening (Fig. 5.4, B). Direct

surface-to-surface comparison of the simulated closed mesh from chord shortening (Fig. 5.9, A, blue surface) to the image of the closed mesh from experiment (Fig. 5.9, B, blue surface) showed mean and maximum error magnitudes of 1.1 and 3.3 mm, respectively (Fig. 5.10, B).

5.3.2 Sensitivity analysis

I conducted a sensitivity analysis to assess the effect of small changes in model parameters on simulation results. Each parameter that affects either mesh geometry or material properties was subject to small positive and negative perturbations, and simulations were run for both cases. The resulting changes in the mean surface-to-surface error magnitude was measured, and sensitivity was computed as

$$S = \lim_{\Delta x \rightarrow 0} \frac{\Delta y}{\Delta x / x} \quad 5.1$$

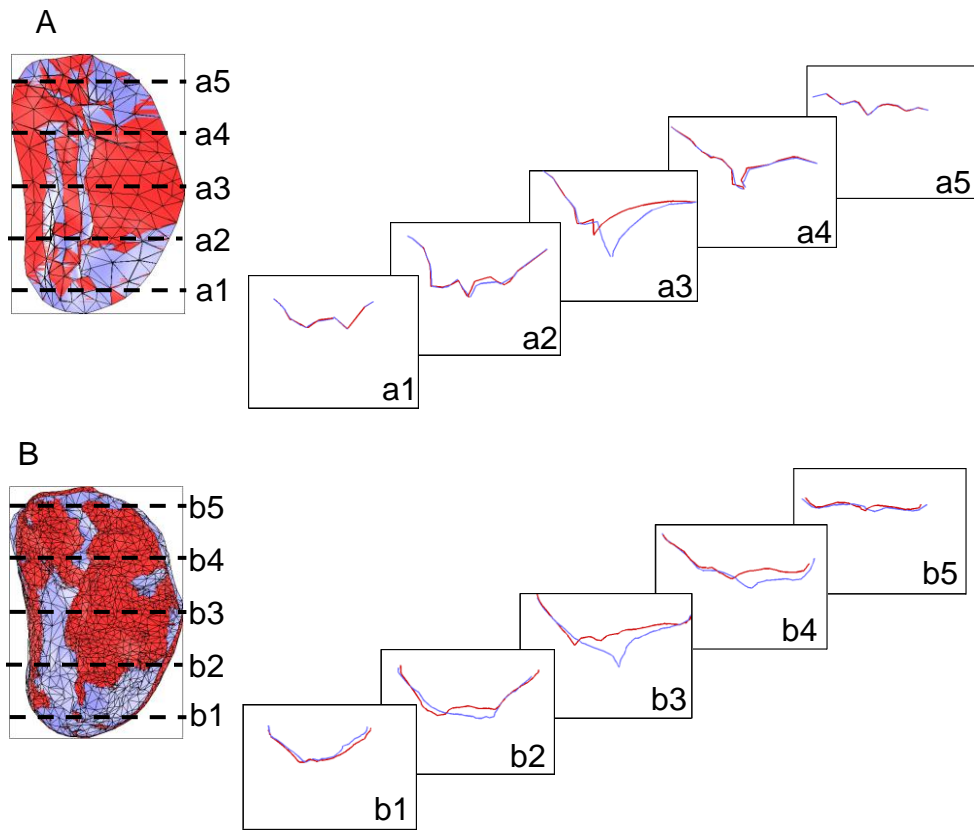


Figure 5.9 (A) Top views of mesh produced from simulations of valve 3 before (red) and after (blue) shortening a posterior leaflet chord using a suture. Panels a1-a5 show cross sections of the two overlaid meshes, with the red and blue curves corresponding to meshes before and after chord shortening, respectively. (B) Top views of mesh produced from image of valve 3 before (red) and after (blue) shortening a posterior leaflet chord using a suture. Panels b1-b5 show cross sections of the two overlaid meshes, with the red and blue curves corresponding to meshes before and after chord shortening, respectively.

where y is the mean magnitude of surface-to-surface error in mm, x is a given model parameter, and S is sensitivity in units of mm per 100% change in model parameter, x . Model parameter perturbations of $\pm 5\%$ were used, and the resulting sensitivity values were expressed in the form of a bar graph (Fig. 5.11).

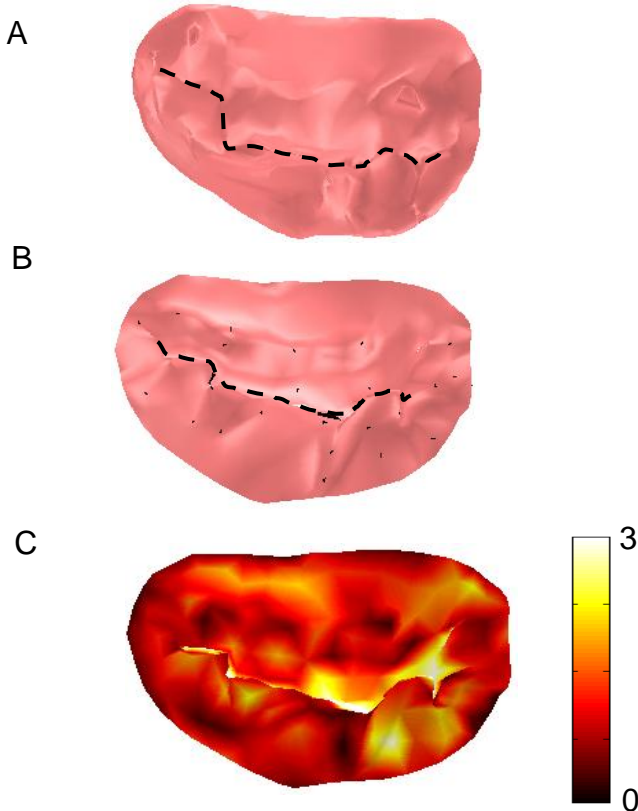


Figure 5.10 (A) Top view of mesh produced directly from image of closed valve 3 after experimentally shortening a posterior leaflet chord. (B) Top view of mesh of valve 3 produced by simulating valve closure after simulated chord shortening. (C) Magnitude of error (distance in mm) between closed mesh produced by simulation and mesh produced directly from closed image.

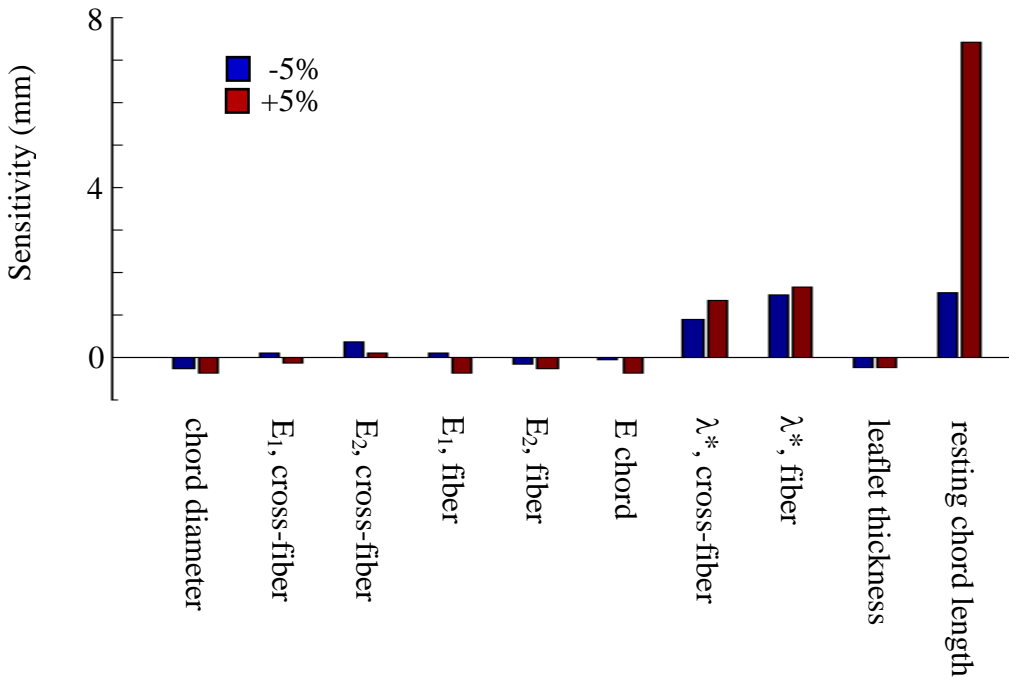


Figure 5.11 Sensitivity of simulation accuracy to model parameters.

Sensitivity is defined here as the change in mean surface error magnitude (in mm) divided by the fractional change in model parameter. For this plot, the input parameters listed on the horizontal axis were varied by negative and positive 5% (blue and red bars, respectively).

5.3.3 Mesh size analysis

The effect of mesh size on simulation accuracy was assessed by subdividing the triangles of valve 3 by factors of 4 and 16 and simulating closure. The simulated closed meshes were superimposed on the mesh produced directly from the image of the closed valve (Fig. 5.12A, C, and E), and error maps were produced (Fig. 5.12B, D and F). The mean and maximum errors for the mesh that was subdivided by 4 were 0.9 and 2.9 mm, respectively, and the mean and

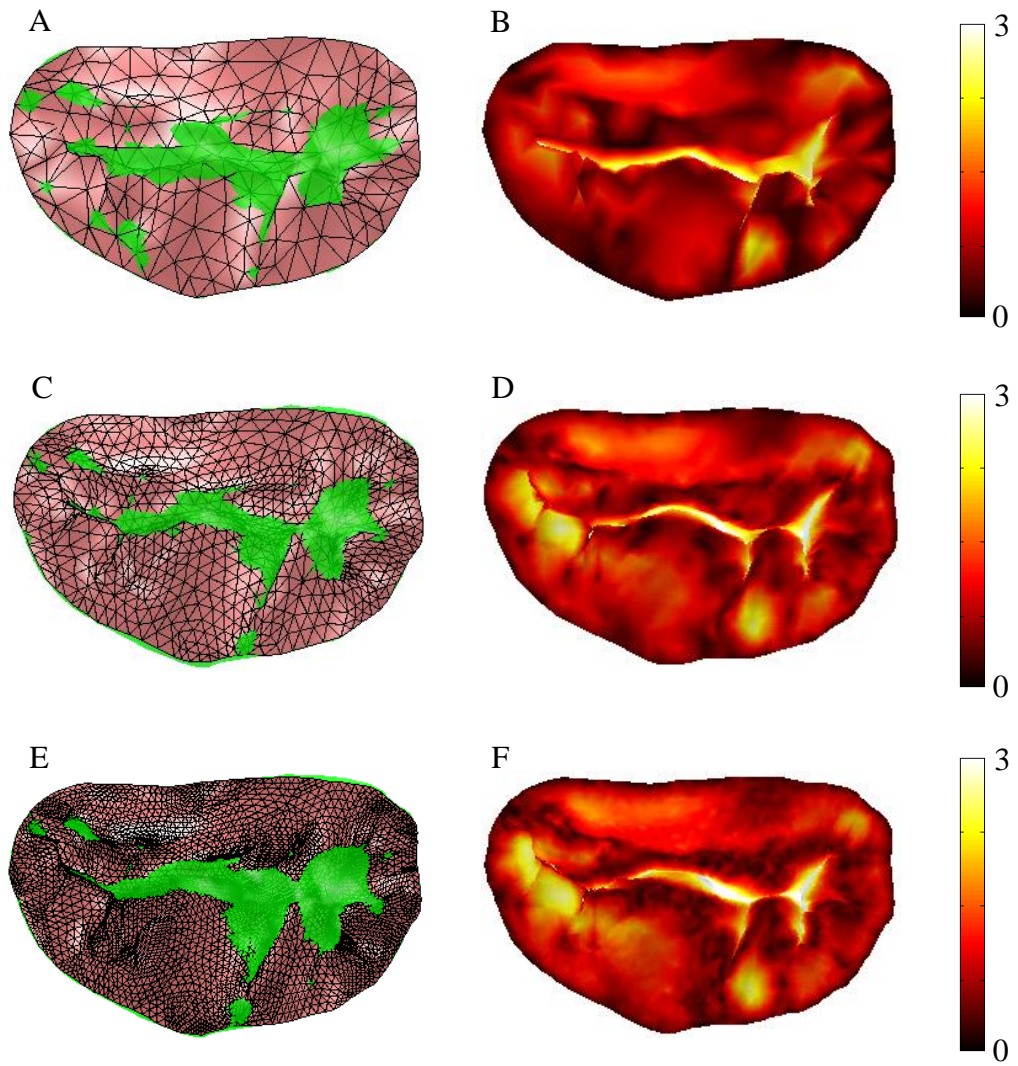


Figure 5.12. Effect of mesh size on simulation accuracy. Panels (A, C, E): Meshes of valve 3 in the closed state (pink) are superimposed on the mesh produced from the image of closed valve surface (shown in green with triangle edges hidden). Panels (B, D, F): Error expressed as the magnitude of the distance between the surfaces in mm. Meshes in panels (A-B), (C-D), and (E-F) contain approximately 625, 2500, and 10000 triangles, respectively.

maximum errors for the mesh that were subdivided by 16 were 0.9 and 2.7 mm, respectively. Simulation times for the meshes that were subdivided by 4 and 16 were 103 and 1240 seconds, respectively.

5.4 Discussion

The aim of this study was to develop a method for producing clinically-oriented simulations of mitral valve closure for use in planning surgical repair. I showed that it was possible to take an image of a mitral valve and from it develop a model that could be used to quickly and accurately predict the closed and loaded state. Furthermore I showed that method could be used to successfully predict the effect of a surgical repair technique.

A major requirement guiding the development of the simulation methods was that the closed and loaded state of the valve be computed quickly through judicious use of approximation. For the three mitral valve specimens simulated in this study, the closed, loaded state was computed in less than 30 seconds using an anisotropic M-S model with efficient contact handling and bilinear approximation of published material constitutive laws. While the M-S method gains much of its speed advantage by neglecting to adhere to a true continuum description of tissue, results of Chapter 3 showed that these approximations result in accurate results for simulation of pressurized membranes. To justify the extension of the M-S model to the pressurized mitral valve, we used image-based validation to assess

accuracy. Another significant approximation is the use of relatively coarse meshes. However, increasing the number of triangular faces in the mesh did not improve the accuracy with which the simulated closed surface approximated the actual closed valve surface. Increasing mesh size slightly improved mesh closure near the coaptation line, but it also led to slightly more billowing in the leaflet bellies (Fig. 5.12).

A second requirement guiding the development of simulation methods was that model geometry be based directly on images of the valve. Despite rapid advances in medical imaging, it is still not possible to resolve the intricate structures of the mitral valve, particularly the full chordae network, from clinical images. I chose to use an experimental imaging method – micro-CT and pressurization with air – rather than a clinically applicable method in order to develop highly detailed geometric models that make it possible to assess the importance of various aspects of model detail for accurate valve simulation. Results suggest that details of the chordae network are important determinants of the closed valve state predicted by the model. The sensitivity analysis shows that simulation accuracy is strongly dependent on the rest lengths of the chordae. In addition, simulations in which secondary chords were omitted showed very large increases in model error, corroborating that the chordae strongly influence closed valve shape.

Model results are fairly insensitive to model parameter variation, with changes in mean surface error of less than one millimeter resulting from a 100% change in

most model parameters. The only parameters other than resting chord length exhibiting sensitivity of greater than one mm were the critical stretch ratios used in the bilinear approximations to the leaflet constitutive law. The critical stretch ratio represents the deflection at which spring stiffness changes, and for the parameters used in this study, stiffness jumps by more than two orders of magnitude at the critical stretch ratio. So increasing one of the critical stretch ratios by, for example, 25% causes all springs associated with that direction to be approximately 25% longer when the leaflet is under systolic pressure load. Thus, it is not surprising that these parameters would strongly influence closed leaflet shape. It is important to note that some important model features are not easily parameterized and hence were not included in the sensitivity analysis. For example, the location of the mitral annulus, which could potentially be difficult to determine from clinical images, may strongly influence closed valve shape.

Direct, image-based validation is an important part of this study. It provides a way to assess accuracy of the whole modeling and simulation process from end to end. This is helpful for this study because of the difficulty in quantifying all of the potential sources of error individually. These include variability in valve tissue properties (both in terms of heterogeneity within a valve and between specimens), errors in extracting valve geometry from images, and errors due to approximations used by the simulation methods. Only two groups have published mitral valve models that incorporate image-based models of the leaflets. Wenk et al developed a FE model of the LV with mitral valve based on MRI images [47].

Their leaflet model was formed from an image of the valve at the closed state, so their model leaflet surface was effectively fused at the interleaflet clefts. They also neglected to model leaflet contact and assumed a generic model of the chordae network since the chordae could not be seen on the MRI images. Burlina et al have also presented an image-based model of the mitral valve leaflets based on 3D ultrasound [48]. They meshed the leaflets in the open state and used simulation to predict the closed state. They could not discern chordae in the ultrasound images, so they incorporated tethering forces at selected nodes on the leaflet free edge and neglected the effects of secondary chordae. They used direct image-based validation to assess the accuracy of simulations and found an average discrepancy between closed models and images of closed valves of four to five mm. Their levels of mean error are five to six times higher than those achieved in this study, probably due to the combination of lower intrinsic resolution to their imaging modality and their absence of secondary chordae in their model.

Although the mitral valve modeling methods presented in this work produce dynamic simulations, I use only a single state of the valve closing cycle – the state of the valve under peak systolic pressure load – to assess whether a valve leaks. One justification for this is that the transvalvular gradient at peak systole represents the greatest mechanical challenge to valve structures and a worst-case scenario for inducing a leak. An additional, more clinical justification for this simplification is that surgeons rely on a passive inflation technique at the end of

surgery to test the repaired valve by injecting saline under static pressure into the LV [14]. The assumption that it is sufficient to assess valve function at peak systolic pressure allows the complex interaction between blood flow and the valve structures during ventricular filling and ejection to be neglected. Despite neglecting the effects of blood flow, simulation time between the beginning of mitral valve closure and the final, fully loaded state was typically about 80 ms, which agrees with measured values of mitral valve closure time determined by cardiac ultrasound [110].

It is important to note that during *in vivo* valve closure, peak systolic pressure is accompanied by LV contraction and an associated decrease in annulus size. It is likely that this brings more leaflet surface into approximation when the valve is closed and facilitates leaflet coaptation. Passive inflation of the LV does the opposite, thus a valve that closes completely during passive inflation will probably close with even greater coaptation under *in vivo* conditions. In this way, the testing of a valve under passive pressurization represents a more stringent test of competency than testing under physiological closure.

In the mitral valve, as in the aortic valve, quality of valve closure can be assessed by the extent of overlap between adjacent leaflets. This could easily be computed from simulation results, but the two leaflets in the coaptation region could not be distinguished in the images of the closed valves, making it impossible for image-based validate of simulations using that metric. This is an

important issue to be addressed, because coaptation height is a measure with real clinical relevance. It is possible that a dynamic imaging modality would provide information to help distinguish the two leaflets by showing the state of the leaflets immediately before or after they are in contact.

A limitation of this work is that the imaging method used to construct the models is not clinically applicable. In fact, despite the high level of leaflet and chordae detail provided by micro-CT under static air loading, it was still difficult to see the complete chordae network, particularly in commissural regions where many chord segments attach to the leaflets in close proximity in the closed valve. These chordae could perhaps be better visualized using an imaging modality with gated acquisition, which might allow chordae on opposing leaflets to be distinguished by looking at points in the cycle just before or after complete closure.

The M-S method used to model leaflet deformation is not a continuum model and does not provide information on stresses in the leaflets. However, predicting complete valve shape at closure, not leaflet stress, was the goal of the study. Currently, surgical repair of the mitral valve is guided by the single criterion that the valve closes completely. Consideration of stresses is necessarily secondary because a repair strategy with a theoretically favorable stress profile, but that fails to close completely, is a failure.

A final limitation is that the mitral valve models developed in this study were porcine rather than human valves. The porcine valve was shown to be an appropriate surrogate for the human valve in a study that showed that valve leaflet dimensions and chord lengths were not significantly different between human and porcine valves [49]. In future studies, it may be possible to create models directly from preoperative clinical images, and, if sufficient details of the actual surgery can be recorded, the repair could be simulated and validated retrospectively against postoperative images. However, this approach hinges on the ability to extract chord anatomy, which I have shown to be important for accurately simulating the closed state of the valve, from clinical images.

While the mitral valve simulations that I presented were image-based models developed for the purpose of studying patient-specific valve repair, the simulation tools could also be used to compare general mitral valve repair strategies. For example, in the case of mitral regurgitation due to a ruptured chord, simulations could be used to compare various repair techniques at the surgeon's disposal – e.g., chord replacement, chord transfer or leaflet resection – individually or in combination.

6 Conclusions and future work

I have developed a modular set of computational tools for simulating the closure and mechanical loading of heart valves for use in planning heart valve surgery. This set of tools allows the choice of a fast but approximate method for intraoperative surgical planning, where very fast simulation is critical, and a more accurate but slower method for preoperative surgical planning, where time constraints are not as limiting. The modular nature of these tools allows the same problem to be analyzed with both methods to quantify how much the approximations affect relevant information predicted by the simulation. By using both methods to simulate the loading of the normal aortic valve, I showed that the M-S model is able to estimate the large displacement and large deformation of pressurized valve leaflets with high overall accuracy despite local regions of relatively high error due to the poor ability of the M-S model to estimate the response to leaflet shear stress.

The specific contribution of this work to simulation methods is that it is the first to use a M-S model in a demanding biomechanics application. The M-S model was able to simulate the nonlinear, anisotropic heart valve leaflets with complex geometry undergoing large deformation and extensive self-contact. Direct image-based validation, as well as direct comparison with a FE membrane model, provided two different ways to assess simulation accuracy

Judicious use of approximation allows computation times to be reduced to levels that make simulation-based surgical planning feasible using relatively modest computing power. Perhaps the most significant approximation contained in my simulations is the M-S model of the mechanical response of valve leaflets. I showed that a computationally and conceptually simple M-S model could accurately reproduce the normal stress-strain response of highly anisotropic and nonlinear tissue. I also quantified the computational advantage to this method over an efficient FE approach. The M-S method, coupled with a fast implicit solver and efficient contact handling, was able to simulate the movement of the valve from the open state to the closed and fully loaded state in less than half of a minute with sub-millimeter mean accuracy.

The modeling tools presented in this work have proven to be able to address questions that solve immediate clinical needs. The FE simulations of aortic valve repair using grafts made of pericardium have provided useful information for guiding clinical practice. The FE model of the aortic valve has also served as a tool for discovering principles of normal valve function. When simulations of the normal aortic valve lacked important physiological features, a reexamination of model assumptions led to the observation of obliquely oriented fibers in the leaflets. An understanding of this fiber arrangement could benefit valve repair as well as the design of bioprosthetic and tissue engineered replacement valves.

While this work has resulted in tools for bringing patient-specific surgical planning of heart valve repair closer to clinical use, several important tasks remain. The first concerns building computational meshes from medical images. I deliberately chose to use a high resolution, high contrast imaging method in order to focus primarily on simulation. Work is ongoing in our lab to extract valve anatomy from 3d ultrasound images resulting in published methods for mitral valve annulus and leaflet segmentation [111]. Segmentation of chordae, however, remains an outstanding challenge, and the results of my analysis of chordae function suggest that chordae imaging must be improved in order to produce image-based models capable of accurate surgical planning.

Another important extension to the current valve simulation environment is the development of a proper computer interface for interacting with the valve mesh for inputting a potential repair strategy. The mitral valve repair that I simulated in Chapter 5 was a simple repair technique parameterized by a single number – the new length of a shortened chord – but a surgical planning system must incorporate a broader range of techniques at the surgeon’s disposal. These include annuloplasty, leaflet resection, and transfer of chordae and papillary muscles.

In order to broaden the pathologies to which surgical simulation can be applied, mechanical properties of diseased valves must be considered. The leaflets of diseased valves can exhibit altered thickness, abnormal in-plane stiffness, and elevated bending stiffness. The biomechanical testing of these diseased valve

tissues remains relatively unexplored. The increased bending stiffness which is likely to accompany several common forms of valve disease presents important challenges that would require enhancements to the modeling methods used in my work. Bending springs would have to be added to the M-S model, incurring additional computational cost. The FE models described here is a membrane formulation, and does not include enough nodal degrees of freedom to handle bending. Shell elements would be more appropriate.

The computational approaches used in this work have not utilized parallel programming strategies. There has been rapid technological growth in both multiple core central processing units and highly parallel general purpose graphics processing units. It is likely that valve simulations can be further accelerated using parallel computing strategies. It is possible that explicit numerical integrations methods, which I deliberately passed over in favor of implicit methods, could be as fast or faster due to their inherent suitability for parallelization. In fact, it might be possible to implement M-S model simulations at real-time rates, allowing virtual surgery simulations with haptic feedback.

Appendix

Numerical solution of equations of motion

Dynamics of a membrane represented by a triangulated mesh can be simulated by lumping the mass of each triangle at the nodes then solving for the dynamics of the system of masses, which can be expressed in state-space form as

$$\begin{pmatrix} \vec{\dot{x}} \\ \vec{\dot{v}} \end{pmatrix} = \begin{pmatrix} \vec{v} \\ M^{-1} \vec{f} \end{pmatrix} \quad \text{A.1}$$

where x and v are vectors of nodal positions and velocities, respectively, M^{-1} is the inverse mass matrix (a diagonal matrix with the reciprocal of nodal mass on the main diagonal), and f is the vector of net nodal force due to internal, external and damping forces. Implicit integration was chosen to enable large integration step sizes [112]. I discretized equation A.1 using a second-order backward-difference formula as

$$\frac{1}{h} \begin{pmatrix} 1.5\vec{x}^{n+1} - 2\vec{x}^n + 0.5\vec{x}^{n-1} \\ 1.5\vec{v}^{n+1} - 2\vec{v}^n + 0.5\vec{v}^{n-1} \end{pmatrix} = \begin{pmatrix} \vec{v}^{n+1} \\ M^{-1} \vec{f}^{n+1} \end{pmatrix} \quad \text{A.2}$$

where h is the integration time step. The net nodal force at step $n+1$ depends on the nodal positions at step $n+1$ making the set of equations nonlinear. It can be linearized by replacing f at step $n+1$ with a first-order Taylor series approximation

$$\vec{f}^{n+1} = \vec{f}^n + \frac{\partial \vec{f}}{\partial \vec{x}} (\vec{x}^{n+1} - \vec{x}^n) + \frac{\partial \vec{f}}{\partial \vec{v}} (\vec{v}^{n+1} - \vec{v}^n) \quad \text{A.3}$$

Following a method used in a study simulating the behavior of cloth [81], equations 3.5 and 3.6 can be combined and expressed as the linear system

$$\begin{aligned} \left(I - \frac{2}{3} h M^{-1} \frac{\partial \vec{f}}{\partial \vec{v}} - \frac{4}{9} h^2 M^{-1} \frac{\partial \vec{f}}{\partial \vec{x}} \right) (\vec{x}^{n+1} - \vec{x}^n) &= \frac{1}{3} (\vec{x}^n - \vec{x}^{n-1}) + \frac{h}{9} (8\vec{v}^n - \\ 2\vec{v}^{n-1}) + \frac{4}{9} h^2 M^{-1} \left(\vec{f}^n - \frac{\partial \vec{f}}{\partial \vec{v}} \vec{v}^n \right) - \frac{2}{9} h M^{-1} \frac{\partial \vec{f}}{\partial \vec{v}} (\vec{x}^n - \vec{x}^{n-1}) \end{aligned} \quad \text{A.4}$$

The Jacobian matrix expressing the partial derivative of the net force vector with respect to velocity is an $N \times N$ block matrix where N is the number of nodes in the system, and each block is 3×3 . Neither internal forces (those due to material deformation) nor those due to applied pressure depend explicitly on nodal velocity, so their contributions are zero. Only the viscous damping term depends on nodal velocity, and its partial derivative yields $-bI$ where b is the damping coefficient and I is the $3N \times 3N$ identity matrix.

The Jacobian matrix expressing the partial derivative of the net force vector with respect to position is also an $N \times N$ block matrix where N is the number of nodes in the system, and each block is 3×3 . For a mass-spring model with a linear spring connecting nodes i and j , elements of the Jacobian are computed as

$$\frac{\partial \vec{f}_i}{\partial \vec{x}_i} = \frac{\partial \vec{f}_j}{\partial \vec{x}_j} = J \quad A.5$$

and

$$\frac{\partial \vec{f}_i}{\partial \vec{x}_j} = \frac{\partial \vec{f}_j}{\partial \vec{x}_i} = -J \quad A.6$$

where

$$J = \begin{pmatrix} l(r - s_x^2) - r^{1.5} & -ls_x s_y & -ls_x s_z \\ -ls_x s_y & l(r - s_y^2) - r^{1.5} & -ls_y s_z \\ -ls_x s_z & -ls_y s_z & l(r - s_z^2) - r^{1.5} \end{pmatrix} \quad A.7$$

For the finite deformation membrane finite element model used in this work, the Jacobian is given in the paper by Taylor et al that presented the original formulation of the membrane FE model [92].

Constraining the boundary nodes

Mesh nodes corresponding to either the annulus of the mitral valve or to the points where chordae insert into the papillary muscles are treated as zero-displacement boundary conditions. This constraint is incorporated into the dynamic simulation by inserting zeros into the inverse mass matrix for each 3 x 3 block along the main diagonal corresponding to the nodes to be constrained. This effectively makes the mass of those nodes infinite so that they undergo no acceleration regardless of the forces that act on them [112].

References

- [1] V. T. Nkomo, J. M. Gardin, T. N. Skelton, J. S. Gottdiener, C. G. Scott and M. Enriquez-Sarano, "Burden of valvular heart diseases: a population-based study," *Lancet*, vol. 368, pp. 1005-1011, Sep 16, 2006.
- [2] W. Rosamond, K. Flegal, G. Friday, K. Furie, A. Go, K. Greenlund, N. Haase, M. Ho, V. Howard, B. Kissela, S. Kittner, D. Lloyd-Jones, M. McDermott, J. Meigs, C. Moy, G. Nichol, C. J. O'Donnell, V. Roger, J. Rumsfeld, P. Sorlie, J. Steinberger, T. Thom, S. Wasserthiel-Smoller, Y. Hong and American Heart Association Statistics Committee and Stroke Statistics Subcommittee, "Heart disease and stroke statistics--2007 update: a report from the American Heart Association Statistics Committee and Stroke Statistics Subcommittee," *Circulation*, vol. 115, pp. e69-171, Feb 6, 2007.
- [3] American College of Cardiology/American Heart Association Task Force on Practice Guidelines, Society of Cardiovascular Anesthesiologists, Society for Cardiovascular Angiography and Interventions, Society of Thoracic Surgeons, R. O. Bonow, B. A. Carabello, C. Kanu, A. C. de Leon Jr, D. P. Faxon, M. D. Freed, W. H. Gaasch, B. W. Lytle, R. A. Nishimura, P. T. O'Gara, R. A. O'Rourke, C. M. Otto, P. M. Shah, J. S. Shanewise, S. C. Smith Jr, A. K. Jacobs, C. D. Adams, J. L. Anderson, E. M. Antman, D. P. Faxon, V. Fuster, J. L. Halperin, L. F. Hiratzka, S. A. Hunt, B. W. Lytle, R. Nishimura, R. L. Page and B. Riegel, "ACC/AHA 2006 guidelines for the management of patients with valvular heart disease: a report of the American College of Cardiology/American Heart Association Task Force on Practice Guidelines (writing committee to revise the 1998 Guidelines for the Management of Patients With Valvular Heart Disease): developed in collaboration with the Society of Cardiovascular Anesthesiologists: endorsed by the Society for Cardiovascular Angiography and Interventions and the Society of Thoracic Surgeons," *Circulation*, vol. 114, pp. e84-231, Aug 1, 2006.
- [4] S. Subramanian and M. A. Borger, "Aortic valve reconstruction: current status," *Herz*, vol. 35, pp. 88-93, Mar, 2010.
- [5] A. Vahanian, H. Baumgartner, J. Bax, E. Butchart, R. Dion, G. Filippatos, F. Flachskampf, R. Hall, B. Iung, J. Kasprzak, P. Nataf, P. Tornos, L. Torracca, A. Wenink and Grupo de Trabajo sobre el Tratamiento de las Valvulopatias de la Sociedad Europea de Cardiología, "Guidelines on the management of valvular heart disease," *Rev. Esp. Cardiol.*, vol. 60, pp. 1e-50e, Jun, 2007.
- [6] D. H. Adams and A. C. Anyanwu, "The cardiologist's role in increasing the rate of mitral valve repair in degenerative disease," *Curr. Opin. Cardiol.*, vol. 23, pp. 105-110, Mar, 2008.

- [7] K. A. Eagle and R. R. Baliga, *Practical Cardiology : Evaluation and Treatment of Common Cardiovascular Disorders*. Philadelphia: Lippincott Williams & Wilkins, 2003.
- [8] K. K. Stout and E. D. Verrier, "Acute valvular regurgitation," *Circulation*, vol. 119, pp. 3232-3241, Jun 30, 2009.
- [9] B. Iung, G. Baron, E. G. Butchart, F. Delahaye, C. Gohlke-Barwolf, O. W. Levang, P. Tornos, J. L. Vanoverschelde, F. Vermeer, E. Boersma, P. Ravaud and A. Vahanian, "A prospective survey of patients with valvular heart disease in Europe: The Euro Heart Survey on Valvular Heart Disease," *Eur. Heart J.*, vol. 24, pp. 1231-1243, Jul, 2003.
- [10] M. S. Sacks and A. P. Yoganathan, "Heart valve function: a biomechanical perspective," *Philos. Trans. R. Soc. Lond. B. Biol. Sci.*, vol. 362, pp. 1369-1391, Aug 29, 2007.
- [11] J. F. Obadia, C. Casali, J. F. Chassignolle and M. Janier, "Mitral subvalvular apparatus: different functions of primary and secondary chordae," *Circulation*, vol. 96, pp. 3124-3128, Nov 4, 1997.
- [12] F. Rodriguez, F. Langer, K. B. Harrington, F. A. Tibayan, M. K. Zasio, A. Cheng, D. Liang, G. T. Daughters, J. W. Covell, J. C. Criscione, N. B. Ingels and D. C. Miller, "Importance of mitral valve second-order chordae for left ventricular geometry, wall thickening mechanics, and global systolic function," *Circulation*, vol. 110, pp. II115-22, Sep 14, 2004.
- [13] W. A. Goetz, H. S. Lim, F. Pekar, H. A. Saber, P. A. Weber, E. Lansac, D. E. Birnbaum and C. M. Duran, "Anterior mitral leaflet mobility is limited by the basal stay chords," *Circulation*, vol. 107, pp. 2969-2974, Jun 17, 2003.
- [14] L. H. Cohn, Ed., *Cardiac Surgery in the Adult*. New York: McGraw-Hill, 2008.
- [15] R. F. Rushmer, *Cardiovascular Dynamics*. Philadelphia: Saunders, 1976.
- [16] Y. C. Fung, *Biomechanics : Circulation*. New York: Springer, 1997.
- [17] E. C. Jones, R. B. Devereux, M. J. Roman, J. E. Liu, D. Fishman, E. T. Lee, T. K. Welty, R. R. Fabsitz and B. V. Howard, "Prevalence and correlates of mitral regurgitation in a population-based sample (the Strong Heart Study)," *Am. J. Cardiol.*, vol. 87, pp. 298-304, Feb 1, 2001.
- [18] N. Piazza, P. de Jaegere, C. Schultz, A. E. Becker, P. W. Serruys and R. H. Anderson, "Anatomy of the aortic valvar complex and its implications for

transcatheter implantation of the aortic valve," *Circ. Cardiovasc. Interv.*, vol. 1, pp. 74-81, Aug, 2008.

[19] M. J. Thubrikar, S. P. Nolan, J. Aouad and J. D. Deck, "Stress sharing between the sinus and leaflets of canine aortic valve," *Ann. Thorac. Surg.*, vol. 42, pp. 434-440, Oct, 1986.

[20] WRITING GROUP MEMBERS, D. Lloyd-Jones, R. J. Adams, T. M. Brown, M. Carnethon, S. Dai, G. De Simone, T. B. Ferguson, E. Ford, K. Furie, C. Gillespie, A. Go, K. Greenlund, N. Haase, S. Hailpern, P. M. Ho, V. Howard, B. Kissela, S. Kittner, D. Lackland, L. Lisabeth, A. Marelli, M. M. McDermott, J. Meigs, D. Mozaffarian, M. Mussolini, G. Nichol, V. L. Roger, W. Rosamond, R. Sacco, P. Sorlie, V. L. Roger, T. Thom, S. Wasserthiel-Smoller, N. D. Wong, J. Wylie-Rosett and American Heart Association Statistics Committee and Stroke Statistics Subcommittee, "Heart disease and stroke statistics--2010 update: a report from the American Heart Association," *Circulation*, vol. 121, pp. e46-e215, Feb 23, 2010.

[21] L. P. Dasi, H. A. Simon, P. Sucosky and A. P. Yoganathan, "Fluid mechanics of artificial heart valves," *Clin. Exp. Pharmacol. Physiol.*, vol. 36, pp. 225-237, Feb, 2009.

[22] W. Vongpatanasin, L. D. Hillis and R. A. Lange, "Prosthetic heart valves," *N. Engl. J. Med.*, vol. 335, pp. 407-416, Aug 8, 1996.

[23] E. M. Lee, L. M. Shapiro and F. C. Wells, "Superiority of mitral valve repair in surgery for degenerative mitral regurgitation," *Eur. Heart J.*, vol. 18, pp. 655-663, Apr, 1997.

[24] A. M. Gillinov, C. Faber, P. L. Houghtaling, E. H. Blackstone, B. K. Lam, R. Diaz, B. W. Lytle, J. F. Sabik 3rd and D. M. Cosgrove 3rd, "Repair versus replacement for degenerative mitral valve disease with coexisting ischemic heart disease," *J. Thorac. Cardiovasc. Surg.*, vol. 125, pp. 1350-1362, Jun, 2003.

[25] T. E. David, "Outcomes of mitral valve repair for mitral regurgitation due to degenerative disease," *Semin. Thorac. Cardiovasc. Surg.*, vol. 19, pp. 116-120, Summer, 2007.

[26] R. O. Bonow, B. A. Carabello, K. Chatterjee, A. C. de Leon Jr, D. P. Faxon, M. D. Freed, W. H. Gaasch, B. W. Lytle, R. A. Nishimura, P. T. O'Gara, R. A. O'Rourke, C. M. Otto, P. M. Shah, J. S. Shanewise and American College of Cardiology/American Heart Association Task Force on Practice Guidelines, "2008 focused update incorporated into the ACC/AHA 2006 guidelines for the management of patients with valvular heart disease: a report of the American College of Cardiology/American Heart Association Task Force on Practice Guidelines (Writing Committee to revise the 1998 guidelines for the management

of patients with valvular heart disease). Endorsed by the Society of Cardiovascular Anesthesiologists, Society for Cardiovascular Angiography and Interventions, and Society of Thoracic Surgeons," *J. Am. Coll. Cardiol.*, vol. 52, pp. e1-142, Sep 23, 2008.

[27] F. Langer, D. Aicher, A. Kissinger, O. Wendler, H. Lausberg, R. Fries and H. J. Schafers, "Aortic valve repair using a differentiated surgical strategy," *Circulation*, vol. 110, pp. II67-73, Sep 14, 2004.

[28] R. A. Jonas, "Aortic valve repair for congenital and balloon-induced aortic regurgitation," *Semin. Thorac. Cardiovasc. Surg. Pediatr. Card. Surg. Annu.*, vol. 13, pp. 60-65, 2010.

[29] J. S. Tweddell, A. N. Pelech, P. C. Frommelt, R. D. Jaquiss, G. M. Hoffman, K. A. Mussatto and S. B. Litwin, "Complex aortic valve repair as a durable and effective alternative to valve replacement in children with aortic valve disease," *J. Thorac. Cardiovasc. Surg.*, vol. 129, pp. 551-558, Mar, 2005.

[30] E. A. Bacha, D. B. McElhinney, K. J. Guleserian, S. D. Colan, R. A. Jonas, P. J. del Nido and G. R. Marx, "Surgical aortic valvuloplasty in children and adolescents with aortic regurgitation: acute and intermediate effects on aortic valve function and left ventricular dimensions," *J. Thorac. Cardiovasc. Surg.*, vol. 135, pp. 552-9, 559.e1-3, Mar, 2008.

[31] K. S. Kunzelman, R. P. Cochran, C. Chuong, W. S. Ring, E. D. Verrier and R. D. Eberhart, "Finite element analysis of the mitral valve," *J. Heart Valve Dis.*, vol. 2, pp. 326-340, May, 1993.

[32] K. Kunzelman, M. S. Reimink, E. D. Verrier and R. P. Cochran, "Replacement of mitral valve posterior chordae tendineae with expanded polytetrafluoroethylene suture: a finite element study," *J. Card. Surg.*, vol. 11, pp. 136-45; discussion 146, Mar-Apr, 1996.

[33] M. S. Reimink, K. S. Kunzelman, E. D. Verrier and R. P. Cochran, "The effect of anterior chordal replacement on mitral valve function and stresses. A finite element study," *ASAIO J.*, vol. 41, pp. M754-62, Jul-Sep, 1995.

[34] K. S. Kunzelman, M. S. Reimink and R. P. Cochran, "Annular dilatation increases stress in the mitral valve and delays coaptation: a finite element computer model," *Cardiovasc. Surg.*, vol. 5, pp. 427-434, Aug, 1997.

[35] K. S. Kunzelman, M. S. Reimink and R. P. Cochran, "Flexible versus rigid ring annuloplasty for mitral valve annular dilatation: a finite element model," *J. Heart Valve Dis.*, vol. 7, pp. 108-116, Jan, 1998.

- [36] K. S. Kunzelman, D. W. Quick and R. P. Cochran, "Altered collagen concentration in mitral valve leaflets: biochemical and finite element analysis," *Ann. Thorac. Surg.*, vol. 66, pp. S198-205, Dec, 1998.
- [37] I. S. Salgo, J. H. Gorman 3rd, R. C. Gorman, B. M. Jackson, F. W. Bowen, T. Plappert, M. G. St John Sutton and L. H. Edmunds Jr, "Effect of annular shape on leaflet curvature in reducing mitral leaflet stress," *Circulation*, vol. 106, pp. 711-717, Aug 6, 2002.
- [38] E. Votta, F. Maisano, M. Soncini, A. Redaelli, F. M. Montevercchi and O. Alfieri, "3-D computational analysis of the stress distribution on the leaflets after edge-to-edge repair of mitral regurgitation," *J. Heart Valve Dis.*, vol. 11, pp. 810-822, Nov, 2002.
- [39] F. Dal Pan, G. Donzella, C. Fucci and M. Schreiber, "Structural effects of an innovative surgical technique to repair heart valve defects," *J. Biomech.*, vol. 38, pp. 2460-2471, Dec, 2005.
- [40] D. R. Einstein, P. Reinhall, M. Nicosia, R. P. Cochran and K. Kunzelman, "Dynamic finite element implementation of nonlinear, anisotropic hyperelastic biological membranes," *Comput. Methods Biomed. Engin.*, vol. 6, pp. 33-44, Feb, 2003.
- [41] D. R. Einstein, K. S. Kunzelman, P. G. Reinhall, M. A. Nicosia and R. P. Cochran, "Non-linear fluid-coupled computational model of the mitral valve," *J. Heart Valve Dis.*, vol. 14, pp. 376-385, May, 2005.
- [42] K. H. Lim, J. H. Yeo and C. M. Duran, "Three-dimensional asymmetrical modeling of the mitral valve: a finite element study with dynamic boundaries," *J. Heart Valve Dis.*, vol. 14, pp. 386-392, May, 2005.
- [43] V. Prot, B. Skallerud and G. A. Holzapfel, "Transversely isotropic membrane shells with application to mitral valve mechanics. Constitutive modeling and finite element implementation," *Int. J. Num. Meth. Eng.*, vol. 71, pp. 987-1008, 2007.
- [44] V. Prot, B. Skallerud, G. Sommer and G. A. Holzapfel, "On modelling and analysis of healthy and pathological human mitral valves: two case studies," *J. Mech. Behav. Biomed. Mater.*, vol. 3, pp. 167-177, Feb, 2010.
- [45] E. Votta, F. Maisano, S. F. Bolling, O. Alfieri, F. M. Montevercchi and A. Redaelli, "The Geoform disease-specific annuloplasty system: a finite element study," *Ann. Thorac. Surg.*, vol. 84, pp. 92-101, Jul, 2007.
- [46] E. Votta, E. Caiani, F. Veronesi, M. Soncini, F. M. Montevercchi and A. Redaelli, "Mitral valve finite-element modelling from ultrasound data: a pilot

study for a new approach to understand mitral function and clinical scenarios," *Philos. Transact A. Math. Phys. Eng. Sci.*, vol. 366, pp. 3411-3434, Sep 28, 2008.

[47] J. F. Wenk, Z. Zhang, G. Cheng, D. Malhotra, G. Acevedo-Bolton, M. Burger, T. Suzuki, D. A. Saloner, A. W. Wallace, J. M. Guccione and M. B. Ratcliffe, "First finite element model of the left ventricle with mitral valve: insights into ischemic mitral regurgitation," *Ann. Thorac. Surg.*, vol. 89, pp. 1546-1553, May, 2010.

[48] P. Burlina, C. Sprouse, D. DeMenthon, A. Jorstad, R. Juang, F. Contijoch, T. Abraham, D. Yuh and E. McVeigh, "Patient-specific modeling and analysis of the mitral valve using 3D-TEE," in 2010, pp. 135-146.

[49] K. S. Kunzelman, R. P. Cochran, E. D. Verrier and R. C. Eberhart, "Anatomic basis for mitral valve modelling," *J. Heart Valve Dis.*, vol. 3, pp. 491-496, Sep, 1994.

[50] P. L. Gould and A. Cataloglu, "Stress analysis of the human aortic valve," *Computers & Structures*, vol. 3, pp. 377-384, 1973.

[51] H. N. Sabbah, M. S. Hamid and P. D. Stein, "Mechanical stresses on closed cusps of porcine bioprosthetic valves: correlation with sites of calcification," *Ann. Thorac. Surg.*, vol. 42, pp. 93-96, Jul, 1986.

[52] M. S. Hamid, H. N. Sabbah and P. D. Stein, "Influence of stent height upon stresses on the cusps of closed bioprosthetic valves," *J. Biomech.*, vol. 19, pp. 759-769, 1986.

[53] M. M. Black, I. C. Howard, X. Huang and E. A. Patterson, "A three-dimensional analysis of a bioprosthetic heart valve," *J. Biomech.*, vol. 24, pp. 793-801, 1991.

[54] S. Krucinski, I. Vesely, M. A. Dokainish and G. Campbell, "Numerical simulation of leaflet flexure in bioprosthetic valves mounted on rigid and expansile stents," *J. Biomech.*, vol. 26, pp. 929-943, Aug, 1993.

[55] M. A. Thornton, I. C. Howard and E. A. Patterson, "Three-dimensional stress analysis of polypropylene leaflets for prosthetic heart valves," *Med. Eng. Phys.*, vol. 19, pp. 588-597, Sep, 1997.

[56] G. Cacciola, G. W. Peters and P. J. Schreurs, "A three-dimensional mechanical analysis of a stentless fibre-reinforced aortic valve prosthesis," *J. Biomech.*, vol. 33, pp. 521-530, May, 2000.

[57] F. L. Xiong, W. A. Goetz, C. K. Chong, Y. L. Chua, S. Pfeifer, E. Wintermantel and J. H. Yeo, "Finite element investigation of stentless pericardial

aortic valves: relevance of leaflet geometry," *Ann. Biomed. Eng.*, vol. 38, pp. 1908-1918, May, 2010.

[58] W. Sun, A. Abad and M. S. Sacks, "Simulated bioprosthetic heart valve deformation under quasi-static loading," *J. Biomech. Eng.*, vol. 127, pp. 905-914, Nov, 2005.

[59] H. Kim, J. Lu, M. S. Sacks and K. B. Chandran, "Dynamic simulation pericardial bioprosthetic heart valve function," *J. Biomech. Eng.*, vol. 128, pp. 717-724, Oct, 2006.

[60] K. J. Grande, R. P. Cochran, P. G. Reinhall and K. S. Kunzelman, "Stress variations in the human aortic root and valve: the role of anatomic asymmetry," *Ann. Biomed. Eng.*, vol. 26, pp. 534-545, Jul-Aug, 1998.

[61] K. J. Grande, R. P. Cochran, P. G. Reinhall and K. S. Kunzelman, "Mechanisms of aortic valve incompetence: finite element modeling of aortic root dilatation," *Ann. Thorac. Surg.*, vol. 69, pp. 1851-1857, Jun, 2000.

[62] K. J. Grande-Allen, R. P. Cochran, P. G. Reinhall and K. S. Kunzelman, "Finite-element analysis of aortic valve-sparing: influence of graft shape and stiffness," *IEEE Trans. Biomed. Eng.*, vol. 48, pp. 647-659, Jun, 2001.

[63] A. Beck, M. J. Thubrikar and F. Robicsek, "Stress analysis of the aortic valve with and without the sinuses of valsalva," *J. Heart Valve Dis.*, vol. 10, pp. 1-11, Jan, 2001.

[64] K. H. Lim, J. Candra, J. H. Yeo and C. M. Duran, "Flat or curved pericardial aortic valve cusps: a finite element study," *J. Heart Valve Dis.*, vol. 13, pp. 792-797, Sep, 2004.

[65] J. Li, X. Y. Luo and Z. B. Kuang, "A nonlinear anisotropic model for porcine aortic heart valves," *J. Biomech.*, vol. 34, pp. 1279-1289, Oct, 2001.

[66] R. Gnyaneshwar, R. K. Kumar and K. R. Balakrishnan, "Dynamic analysis of the aortic valve using a finite element model," *Ann. Thorac. Surg.*, vol. 73, pp. 1122-1129, Apr, 2002.

[67] A. Ranga, R. Mongrain, Y. Biadilah and R. Cartier, "A compliant dynamic FEA model of the aortic valve," in Proceedings 12th IFToMM World Congress, Besançon (France), June 18-21, 2007.

[68] C. A. Conti, E. Votta, A. Della Corte, L. Del Viscovo, C. Bancone, M. Cotrufo and A. Redaelli, "Dynamic finite element analysis of the aortic root from MRI-derived parameters," *Med. Eng. Phys.*, vol. 32, pp. 212-221, Mar, 2010.

- [69] M. A. Nicosia, R. P. Cochran, D. R. Einstein, C. J. Rutland and K. S. Kunzelman, "A coupled fluid-structure finite element model of the aortic valve and root," *J. Heart Valve Dis.*, vol. 12, pp. 781-789, Nov, 2003.
- [70] J. De Hart, G. W. Peters, P. J. Schreurs and F. P. Baaijens, "A three-dimensional computational analysis of fluid-structure interaction in the aortic valve," *J. Biomech.*, vol. 36, pp. 103-112, Jan, 2003.
- [71] C. J. Carmody, G. Burriesci, I. C. Howard and E. A. Patterson, "An approach to the simulation of fluid-structure interaction in the aortic valve," *J. Biomech.*, vol. 39, pp. 158-169, 2006.
- [72] S. Katayama, N. Umetani, S. Sugiura and T. Hisada, "The sinus of Valsalva relieves abnormal stress on aortic valve leaflets by facilitating smooth closure," *J. Thorac. Cardiovasc. Surg.*, vol. 136, pp. 1528-35, 1535.e1, Dec, 2008.
- [73] E. J. Weinberg and M. R. Kaazempur Mofrad, "Transient, three-dimensional, multiscale simulations of the human aortic valve," *Cardiovasc. Eng.*, vol. 7, pp. 140-155, Dec, 2007.
- [74] K. L. Billiar and M. S. Sacks, "Biaxial mechanical properties of the natural and glutaraldehyde treated aortic valve cusp--Part I: Experimental results," *J. Biomech. Eng.*, vol. 122, pp. 23-30, Feb, 2000.
- [75] K. May-Newman and F. C. Yin, "Biaxial mechanical behavior of excised porcine mitral valve leaflets," *Am. J. Physiol.*, vol. 269, pp. H1319-27, Oct, 1995.
- [76] P. E. Hammer, N. V. Vasilyev, D. P. Perrin, P. J. del Nido and R. D. Howe, "Fast image-based model of mitral valve closure for surgical planning," in MICCAI Workshop: Computational Biomechanics for Medicine, pp. 15-26, Sep, 2008.
- [77] H. Kim, K. B. Chandran, M. S. Sacks and J. Lu, "An experimentally derived stress resultant shell model for heart valve dynamic simulations," *Ann. Biomed. Eng.*, vol. 35, pp. 30-44, Jan, 2007.
- [78] V. Prot, R. Haaverstad and B. Skallerud, "Finite element analysis of the mitral apparatus: annulus shape effect and chordal force distribution," *Biomech. Model. Mechanobiol.*, vol. 8, pp. 43-55, Feb, 2009.
- [79] P. N. Watton, X. Y. Luo, X. Wang, G. M. Bernacca, P. Molloy and D. J. Wheatley, "Dynamic modelling of prosthetic chorded mitral valves using the immersed boundary method," *J. Biomech.*, vol. 40, pp. 613-626, 2007.
- [80] E. Votta, A. Arnoldi, A. Invernizzi, R. Ponzini, F. Veronesi, G. Tamborini, M. Pepi, F. Alamanni, A. Redaelli and E. G. Caiani. Mitral valve patient-specific

finite element modeling from 3-D real time echocardiography: A potential new tool for surgical planning. Presented at CI2BM09 - MICCAI Workshop on Cardiovascular Interventional Imaging and Biophysical Modelling, 2009.

[81] K. Choi and H. Ho, "Stable but responsive cloth," *ACM Transactions on Graphics*, vol. 21, pp. 604-611, 2002.

[82] H. Delingette, "Triangular springs for modeling non-linear membranes," *IEEE Transactions on Visualization and Computer Graphics*, vol. 14, pp. 329-341, 2008.

[83] A. Van Gelder, "Approximate simulation of elastic membranes by triangulated spring meshes," *Journal of Graphics Tools*, vol. 3, pp. 21-42, 1998.

[84] S. F. F. Gibson and B. Mirtich, "A survey of deformable modeling in computer graphics," Tech. Rep. TR-97-19, 1997.

[85] G. Bianchi, B. Solenthaler, G. Szekely and M. Harders, "Simultaneous topology and stiffness identification for mass-spring models based on FEM reference deformations," in Medical Image Computing and Computer-Assisted Intervention 2004, pp. 293-301.

[86] O. Deussen, L. Kobbelt and P. Tucke, "Using simulated annealing to obtain good nodal approximations of deformable objects," in Sixth Eurographics Workshop on Simulation and Animation 1995, pp. 30-43.

[87] B. A. Lloyd, G. Szekely and M. Harders, "Identification of spring parameters for deformable object simulation," *IEEE Transactions on Visualization and Computer Graphics*, vol. 13, pp. 1081-1094, 2007.

[88] D. Bourguignon and M. Cani, "Controlling anisotropy in mass-spring systems," *EGCAS*, pp. 113-123, 2000.

[89] Y. C. Fung, *Biomechanics : Mechanical Properties of Living Tissues*. New York: Springer-Verlag, 1993.

[90] M. S. Sacks, "A method for planar biaxial mechanical testing that includes in-plane shear," *J. Biomech. Eng.*, vol. 121, pp. 551-555, Oct, 1999.

[91] D. A. Field, "Qualitative measures for initial meshes," *Int. J. Num. Meth. Eng.*, vol. 47, pp. 887-906, 2000.

[92] R. L. Taylor, E. Oñate and P. Ubach, "Finite element analysis of membrane structures," in *Textile Composites and Inflatable Structures*, E. Oñate and B. Kröplin, Eds. 2005, pp. 47-68.

- [93] W. H. Press, *Numerical Recipes : The Art of Scientific Computing*. Cambridge Cambridgeshire ; New York: Cambridge University Press, 1986.
- [94] R. Barrett, *Templates for the Solution of Linear Systems : Building Blocks for Iterative Methods*. Philadelphia: Siam, 1994.
- [95] C. A. Conti, A. Della Corte, E. Votta, L. Del Viscovo, C. Bancone, L. S. De Santo and A. Redaelli, "Biomechanical implications of the congenital bicuspid aortic valve: a finite element study of aortic root function from in vivo data," *J. Thorac. Cardiovasc. Surg.*, vol. 140, pp. 890-6, 896.e1-2, Oct, 2010.
- [96] E. Keeve, S. Girod, R. Kikinis and B. Girod, "Deformable modeling of facial tissue for craniofacial surgery simulation," *Comput. Aided Surg.*, vol. 3, pp. 228-238, 1998.
- [97] W. D. Merryman, H. Y. Huang, F. J. Schoen and M. S. Sacks, "The effects of cellular contraction on aortic valve leaflet flexural stiffness," *J. Biomech.*, vol. 39, pp. 88-96, 2006.
- [98] I. Vesely and D. Boughner, "Analysis of the bending behaviour of porcine xenograft leaflets and of natural aortic valve material: bending stiffness, neutral axis and shear measurements," *J. Biomech.*, vol. 22, pp. 655-671, 1989.
- [99] J. Georgii and R. Westermann, "Mass-spring systems on the GPU," *Simulation Modelling Practice and Theory*, vol. 13, pp. 693-702, 2005.
- [100] J. Mosegaard, P. Herborg and T. S. Sorensen, "A GPU accelerated spring mass system for surgical simulation," *Stud. Health Technol. Inform.*, vol. 111, pp. 342-348, 2005.
- [101] E. Tejada and T. Ertl, "Large steps in GPU-based deformable bodies simulation," *Simulation Modelling Practice and Theory*, vol. 13, pp. 703-715, 2005.
- [102] C. M. Duran, B. Gometza, N. Kumar, R. Gallo and R. Martin-Duran, "Aortic valve replacement with freehand autologous pericardium," *J. Thorac. Cardiovasc. Surg.*, vol. 110, pp. 511-516, Aug, 1995.
- [103] M. R. Labrosse, K. Lobo and C. J. Beller, "Structural analysis of the natural aortic valve in dynamics: from unpressurized to physiologically loaded," *J. Biomech.*, vol. 43, pp. 1916-1922, Jul 20, 2010.
- [104] H. Kim, J. Lu, M. S. Sacks and K. B. Chandran, "Dynamic simulation of bioprosthetic heart valves using a stress resultant shell model," *Ann. Biomed. Eng.*, vol. 36, pp. 262-275, Feb, 2008.

- [105] M. R. Labrosse, C. J. Beller, F. Robicsek and M. J. Thubrikar, "Geometric modeling of functional trileaflet aortic valves: development and clinical applications," *J. Biomech.*, vol. 39, pp. 2665-2672, 2006.
- [106] M. Swanson and R. E. Clark, "Dimensions and geometric relationships of the human aortic valve as a function of pressure," *Circ. Res.*, vol. 35, pp. 871-882, Dec, 1974.
- [107] M. Thubrikar, *The Aortic Valve*. Boca Raton: CRC Press, 1990.
- [108] D. Baraff, *Dynamic Simulation of Non-Penetrating Rigid Bodies*. Ph. D. Thesis, Computer Science Department, Cornell University, 1992.
- [109] D. L. Logan, *A First Course in the Finite Element Method*. Toronto, Canada: Thomson, 2007.
- [110] S. Saito, Y. Araki, A. Usui, T. Akita, H. Oshima, J. Yokote and Y. Ueda, "Mitral valve motion assessed by high-speed video camera in isolated swine heart," *Eur. J. Cardiothorac. Surg.*, vol. 30, pp. 584-591, Oct, 2006.
- [111] R. J. Schneider, D. P. Perrin, N. V. Vasilyev, G. R. Marx, P. J. del Nido and R. D. Howe, "Mitral annulus segmentation from 3D ultrasound using graph cuts," *IEEE Trans. Med. Imaging*, vol. 29, pp. 1676-1687, Sep, 2010.
- [112] D. Baraff and A. Witkin, "Large steps in cloth simulation," *International Conference on Computer Graphics and Interactive Techniques*, pp. 43-54, 1998.